GEOTECHNICAL EXTREME EVENTS RECONNAISSANCE (GEER) ASSOCIATION

Turning Disaster into Knowledge

Geotechnical Reconnaissance of the 2015 M_w8.3 Illapel, Chile Earthquake

Editors:
Gregory P. De Pascale, Gonzalo Montalva, Gabriel Candia, and Christian Ledezma

Lead Authors:
Gabriel Candia, Universidad del Desarrollo-CIGIDEN; Gregory P. De Pascale, Universidad de Chile; Christian Ledezma, Pontificia Universidad Católica de Chile; Felipe Leyton, Centro Sismológico Nacional; Gonzalo Montalva, Universidad de Concepción; Esteban Sáez, Pontificia Universidad Católica de Chile; Gabriel Vargas Easton, Universidad de Chile.

Contributing Authors:
Juan Carlos Báez, Centro Sismológico Nacional; Christian Barrueto, Pontificia Universidad Católica de Chile; Cristián Benítez, Pontificia Universidad Católica de Chile; Jonathan Bray, UC Berkeley; Alondra Chamorro, Pontificia Universidad Católica de Chile; Tania Cisterna, Universidad de Concepción; Fernando Estéfan Thibodeaux Garcia, UC Berkeley; José González, Universidad de Chile; Diego Inzunza, Universidad de Concepción; Rosita Jünemann, Pontificia Universidad Católica de Chile; Benjamín Ledesma, Universidad de Concepción; Álvaro Muñoz, Pontificia Universidad Católica de Chile; Antonio Andrés Muñoz, Universidad de Chile; José Quiroz, Universidad de Concepción; Francesca Sandoval, Universidad de Chile; Pedro Troncoso, Universidad de Concepción; Carlos Videla, Pontificia Universidad Católica de Chile; Angelo Villalobos, Universidad de Chile.

GEER Association Report No. GEER-043

Version 1: December 10, 2015

FUNDING SOURCES

Funding for the reconnaissance team from PUC, campaign September 23rd-25th was provided by the National Research Center for Integrated Natural Disaster Management CONICYT/FONDAP/15110017. Gabriel Candia was also sponsored by Universidad del Desarrollo. Gregory De Pascale was also sponsored by a Universidad de Chile FCFM academic fund and CEGA FONDAP CONICYT 15090013. Gonzalo Montalva and the Universidad de Concepción group were funded by FONDECYT 11121404 and Water Research Center for Agriculture and Mining CONICYT/FONDAP/15130015. Participation of GEER Steering Committee personnel in coordinating and reviewing the report was made possible by the U.S. National Science Foundation (NSF) through Grant No. CMMI-1266418. Any opinions, findings, and conclusions or recommendations expressed in this material are those of the authors and do not necessarily reflect the views of the NSF.

1. Background on the 16 September 2015 Illapel, Chile Earthquake

The 2015 Illapel earthquake took place in Central Chile along the subduction zone interface. The event triggered a tsunami that damaged structures along the coast while the strong ground motions from the event triggered liquefaction and rockfall. Because of the strong building code for subduction zone events in Chile, damage was limited due to the shaking, although there was widespread damage to single and double story residential homes adjacent to beaches. In total there were 13 fatalities and 6 missing persons after the event, mostly due to the tsunami although an immediate evacuation of over 1 million people likely greatly reduced the impact and casualties of the event.

This report starts with an introduction to the area (below) and the seismological background and is followed by sections on strong ground motions, response of retaining and seafront structures, rockfall, and liquefaction. The GEER team was comprised of members from the Chilean Academic community and fieldwork on the reconnaissance started immediately after the event.

The M_w 8.3 event that affected the Illapel area was triggered at 22:54:32 (UTC) on September 16th of 2015, with hypocentral location 31.5530°S, 71.8640°W, and 8.2 km deep, as reported by the Chilean National Seismological Center (CSN). In the Chilean subduction zone, the oceanic Nazca Plate subducts beneath South America at a current rate of ~66 mm/yr (Angermann et al., 1999), which is slower than its mean rate over the past several million years of ~85 mm/yr (DeMets et al., 1994). North-Central Chile exhibits a semi-arid climate and represents the transition zone between the arid north of Chile and the more humid south of Chile (e.g., Heinze, 2003). The geologic units of Andes in onshore area within the zone of the September 2015 earthquake are Jurassic-Cretaceous, Cretaceous, Upper Cretaceous and K-T igneous and stratified rocks of Late Cenozoic marine and continental sediments (SERNAGEOMIN, 2003). The continental basement here is composed of metamorphic, intrusive, and stratified rocks that range in age from Upper Paleozoic to Jurassic (SERNAGEOMIN, 2003) which are related to the Pre-Andean orogeny. Cenozoic basins and crustal faults are present in the Coastal Cordillera domain and well exposed near the shoreline and Tongoy Bay (e.g., Le Roux et al., 2006; Heinze, 2003). The sedimentary fill of the Cenozoic basins (e.g., Tongoy-Limari basin) is composed of Miocene-Pliocene marine sequences of the Coquimbo Formation (Le Roux et al., 2006), which is overlain by Plio-Pleistocene fluvial sediments, which is separated from the former by an angular unconformity (Heinze, 2003; Martínez, 1979).

Regarding historical major seismicity in the region, the M_w 8.3 Illapel earthquake 2015 was one of a number of >M_w 8 earthquakes that impacted the area in the past three hundred years

(Figure 1.1, after Dura et al., 2015). Importantly, major subduction zone ruptures occurred in the zone of the 2015 Illapel earthquake in 1730, 1822, and 1906 and in 1985. Research suggests (e.g., Dura et al., 2015 and references within) that the area is due for a larger magnitude event, similar to the 1730 event (on the order of magnitude 9.0+).

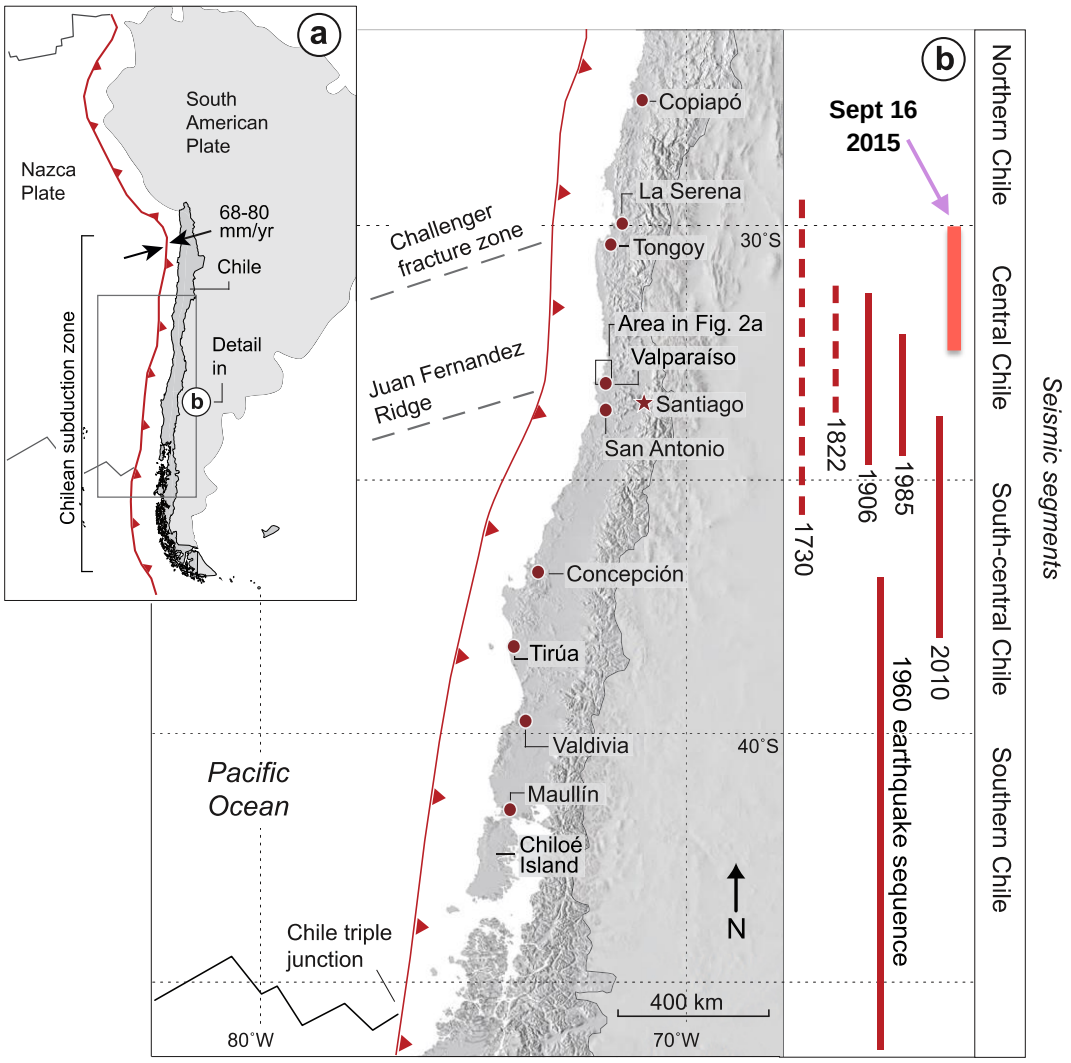

Figure 1.1. Maps showing A) Plate-tectonic setting of Chile and B) estimated rupture lengths of the largest historical earthquakes in central Chile since 1730 compiled from Lomnitz (1970), Kelleher (1972), Comte et al., (1986), Beck et al. (1988) and Melnick et al., (2009). Map after Dura et al. (2015). Note the September 16, 2015 Illapel Earthquake rupture length and the 285 years since the last major earthquake rupture in this area. Note the rupture length of the 2015 Illapel earthquake in orange and how there is not an overlap in rupture areas between the 2010 Maule rupture (see GEER report doi:10.18118/G6NP4W) and the 2015 Illapel Earthquake (this report), which suggests that the region is due for another major event.

Because of the long duration since the last event here, understanding and documenting the geotechnical response of infrastructure, soil, and rock in a smaller event, such as the recent M_w 8.3 Illapel earthquake, enlightens us as to what we may expect during a much larger, 1730-style megathrust earthquake. As it occurred in the Iquique 2014, and Maule 2010 events (Figure 2.1), this earthquake filled a large seismic gap between the 1985 M_w 7.9 Valparaiso earthquake and the 1922 M_w 8.7 event. The gap had previously ruptured on the 1943 M_w 7.9 and the great 1730 M_w 8.7 events, also a relatively minor event the 1880 M_w 7.7 earthquake is reported by Nishenko (1991).

2. Seismological background and recorded ground motions

The M_w 8.3 event that affected the Illapel area was triggered at 22:54:32 (UTC) on September 16th of 2015, with hypocentral location 31.5530°S, 71.8640°W, and 8.2 km deep, as reported by the Chilean National Seismological Center (CSN). As it occurred in the Iquique 2014, and Maule 2010 events, this earthquake filled a large seismic gap (Figure 2.1) between the 1985 M_w 7.9 Valparaiso earthquake and the 1922 M_w 8.7 event. The gap had previously ruptured on the 1943 M_w 7.9 and the great 1730 M_w 8.7 events as well as a relatively minor event, the 1880 M_w 7.7 earthquake as reported by Nishenko (1991). The event was recorded by 17 strong motion stations, and 15 GPS stations. While an important number of aftershocks were triggered, no significant precursor activity is reported.

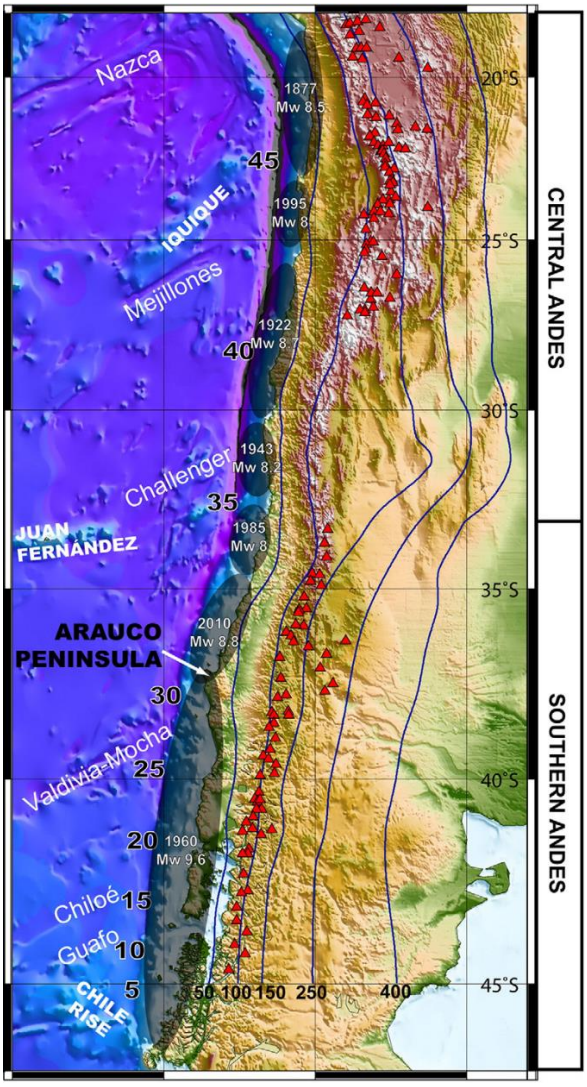

Figure 2.1. Seismic Gap and previous events (Tassara, 2010).

2.1. Foreshock and Aftershock activity

The Illapel area experienced sparse seismicity during the period previous to the Illapel earthquake; Figure 2.2, left, shows the events with M_w greater or equal to 4.5 reported in the area during the 5 months prior to the event. Figure 2.2, right, presents the seismicity reported 6 weeks following the main event. The largest aftershocks, M_w 7.1 and 7.6, took place 5 and 25 minutes after the main event, respectively.

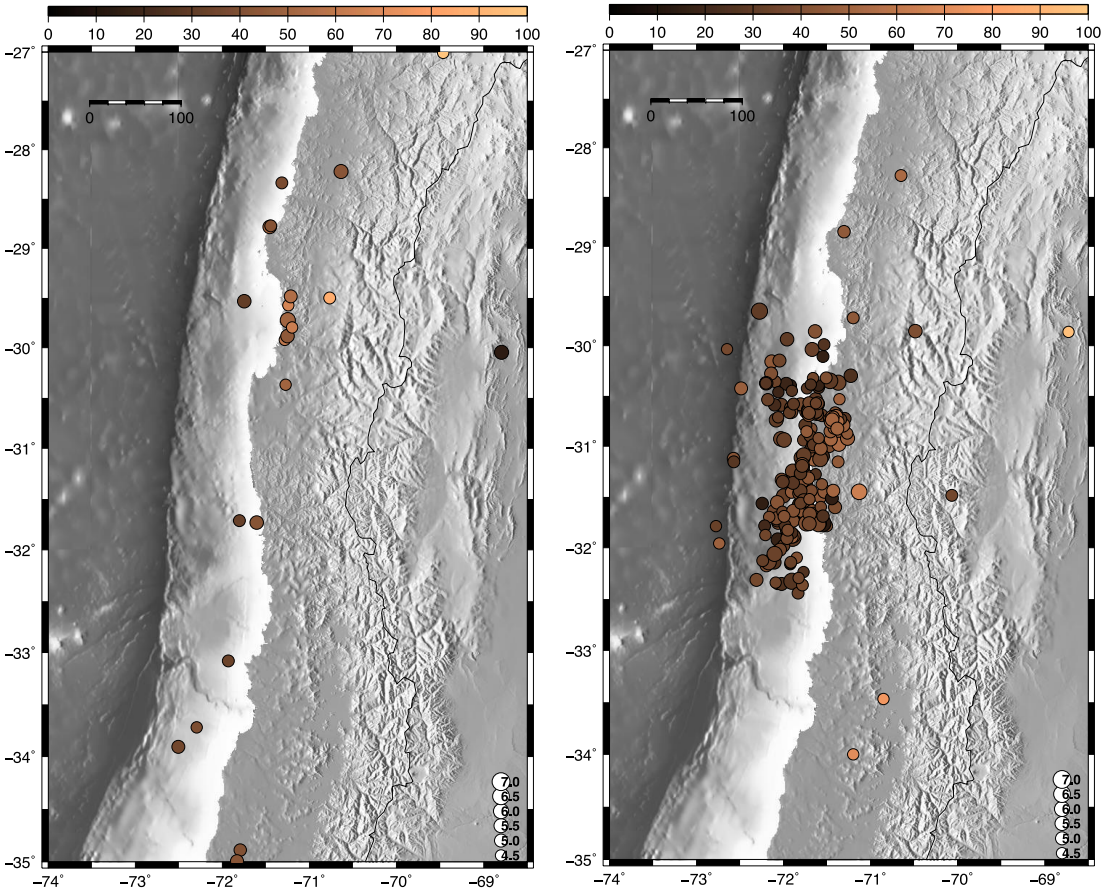

Figure 2.2. Topographic maps showing the seismicity 5 months before the main event (left) and 6 weeks after (right). The color is proportional to the depth, following the scale on the top; while the size is related to the magnitude, according to the scale in the lower right corner.

From Figure 2.2, no clear precursory activity can be observed prior to the main event, with only 22 events of magnitude equal or greater than 4.5. On the other hand, an important aftershock sequence followed the main event, with 219 earthquakes of magnitude ≥ 4.5; from these events, 20 had magnitude larger or equal to 6.0.

2.2. Main Event

Several finite fault solutions are already available for this event. The solution shown in Figure 2.3 (Del Campo and Baez, 2015) is based on the inversion of local GPS stations. As can be seen on the figure, the maximum slip on the rupture exceeds five meters, and permanent displacements of the ground are concentrated between latitudes 29.5°S and 32°S on a 250 km stretch.

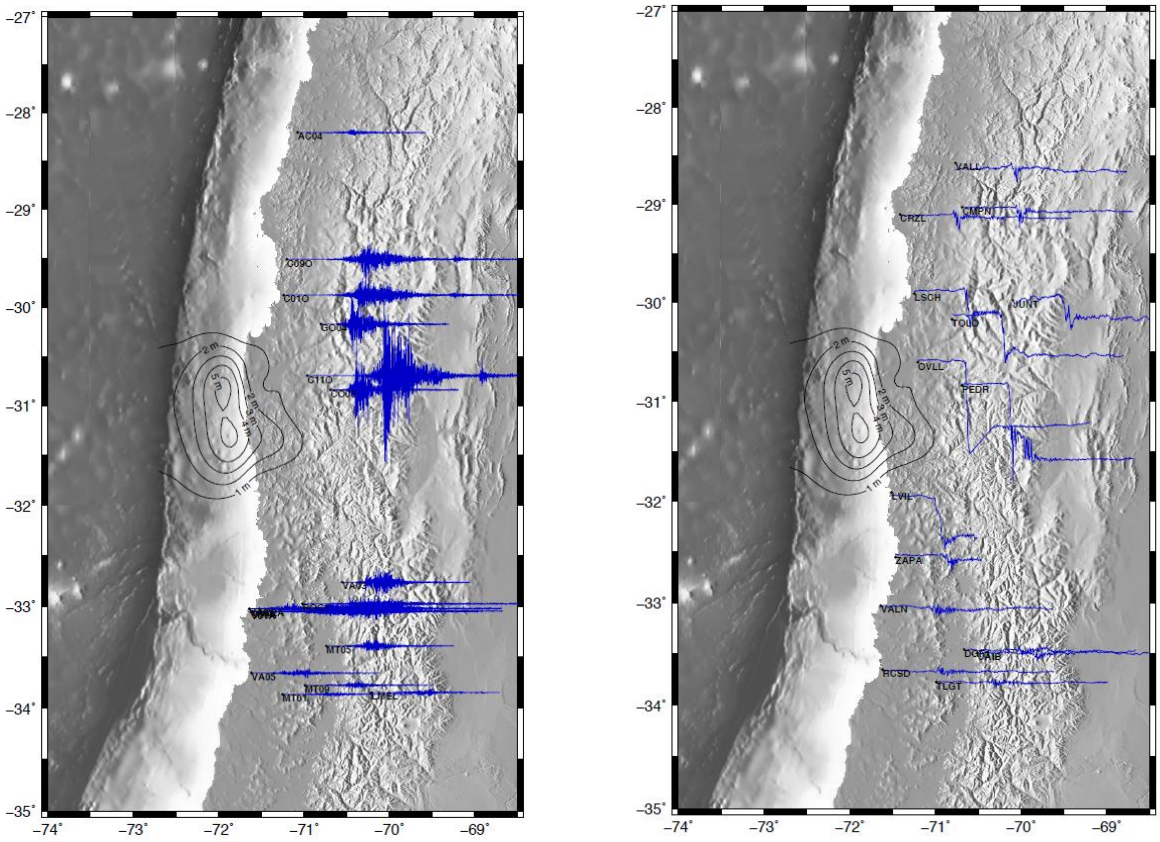

Figure 2.3. Strong motion records (EW component) and kinematic GPS displacements.

2.3. Recorded Ground Motions

The available acceleration records correspond to 17 3-component ground motion (GM) stations plus 15 high frequency GPS measurements. A summary of the main intensity parameters recorded on the GM stations is presented in Table 2.1. These intensities are for the corrected acceleration traces, the records were processed following Bastías and Montalva (2015), and the average upper 30 meter shear-wave velocity (i.e., V_{s30}) was measured during the field campaign or estimated following the same reference. For the stations locations and additional metadata the reader is referred to the cited reference, Figure 2.3, or the CSN website (www.csn.uchile.cl).

Table 2.1 Ground Motion Intensities

Station Code	PGA N-S (g)	PGA E-W (g)	PGA V (g)	PGV (cm/s)		Arias Intensity (m/s)		V_{s30} (m/s)
				N-S	E-W	N-S	E-W	
C11O	0.71	0.83	0.47	32.1	38.3	1081	1471	402
V02A	0.14	0.09	0.05	3.6	4.4	91	88	622
V09A	0.06	0.05	0.03	5.6	5.9	32	26	317
C01O	0.18	0.15	0.12	9.6	10.7	115	99	399
V01A	0.05	0.05	0.02	2.7	4.0	9	13	642
C09O	0.19	0.19	0.09	5.8	8.0	116	91	576
GO04	0.34	0.24	0.16	38.1	31.8	313	252	405
LMEL	0.04	0.03	0.02	2.3	2.2	10	7	808
ROC1	0.05	0.04	0.03	5.4	6.9	23	14	1951*
AC04	0.02	0.03	0.02	2.8	3.9	3	4	583
CO03	0.29	0.35	0.19	13.2	15.7	328	360	639
MT01	0.02	0.02	0.02	1.7	2.2	3	3	727
MT05	0.06	0.06	0.02	4.0	5.0	18	26	496
MT09	0.03	0.03	0.02	2.8	3.1	7	6	1127
VA01	0.05	0.04	0.02	2.5	3.6	14	11	631
VA03	0.09	0.14	0.05	4.8	5.5	50	111	688
VA05	0.03	0.04	0.02	2.1	4.5	8	11	359

(*) Measured V_{s30} value. All the remaining values are inferred following Bastías and Montalva (2015).

An analysis of the strong motion data can be performed in terms of the expected versus the observed surface intensities. Figure 2.4 presents the residuals (i.e., Res = $IM_{obs} - IM_{pred}$) for five intensity measures (IM) presented in natural log units for the 17 GM stations that recorded the main event. The observed values, IM_{obs}, are the geometric mean of the two horizontal components for each GM station, while the predicted intensity, IM_{pred}, is the predicted using the Abrahamson et al. (2015) ground motion prediction model for subduction zones.

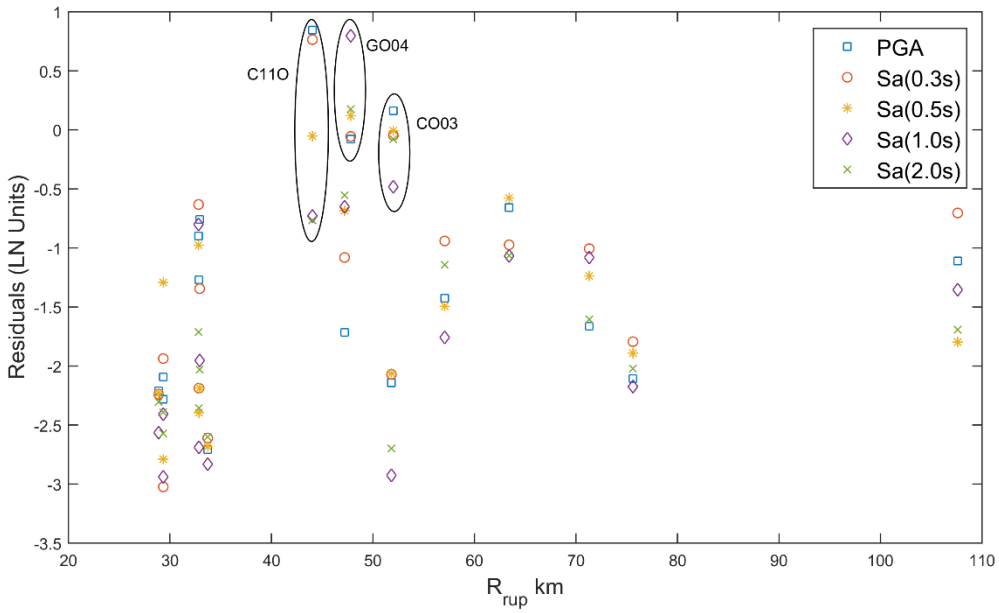

Figure 2.4. Ground Motion Residuals versus Closest Distance (R_{rup}).

The main conclusion from the intensity residuals is that the mean event residual is clearly negative, despite the spectral ordinate. This implies that expected intensities are significantly higher than observed, this is true not only for the Abrahamson et al. (2015) model, but even locally fitted models give the same trend. The reasons as to why this event underperformed in terms of surface intensities are beyond the scope of this report. Observing the residuals station C11O stands as an outlier with positive residuals in high frequencies.

Although the Illapel event was recorded by fewer stations than, for example, the 2014 Iquique earthquake, this event has pairs of accelerometric and GPS stations that recorded the event on the same site (or sufficiently close to compare). This presents a rare opportunity to compare the performance of these two types of instrumentation on a large event with PGAs over 0.8g and rupture slips greater than 6 meters. Figure 2.5 shows the comparison of the integrated acceleration traces with the differentiated displacement traces from the GPS kinematic inversion (Baez, 2015). This takes the traces from both types of instruments to a comparable unit (velocity). Due to space constrains, only two sites are shown herein. The remarkable match of the velocity traces from kGPS with the ones from acceleration (low-pass filtered to 1Hz due to GPS sampling is only 1 Hz) shows the significant improvement made by GPS technology in recent years, and the clear possibility of avoiding the complexities (and uncertainties) that come from long period filtering (e.g., Akkar and Bommer, 2006).

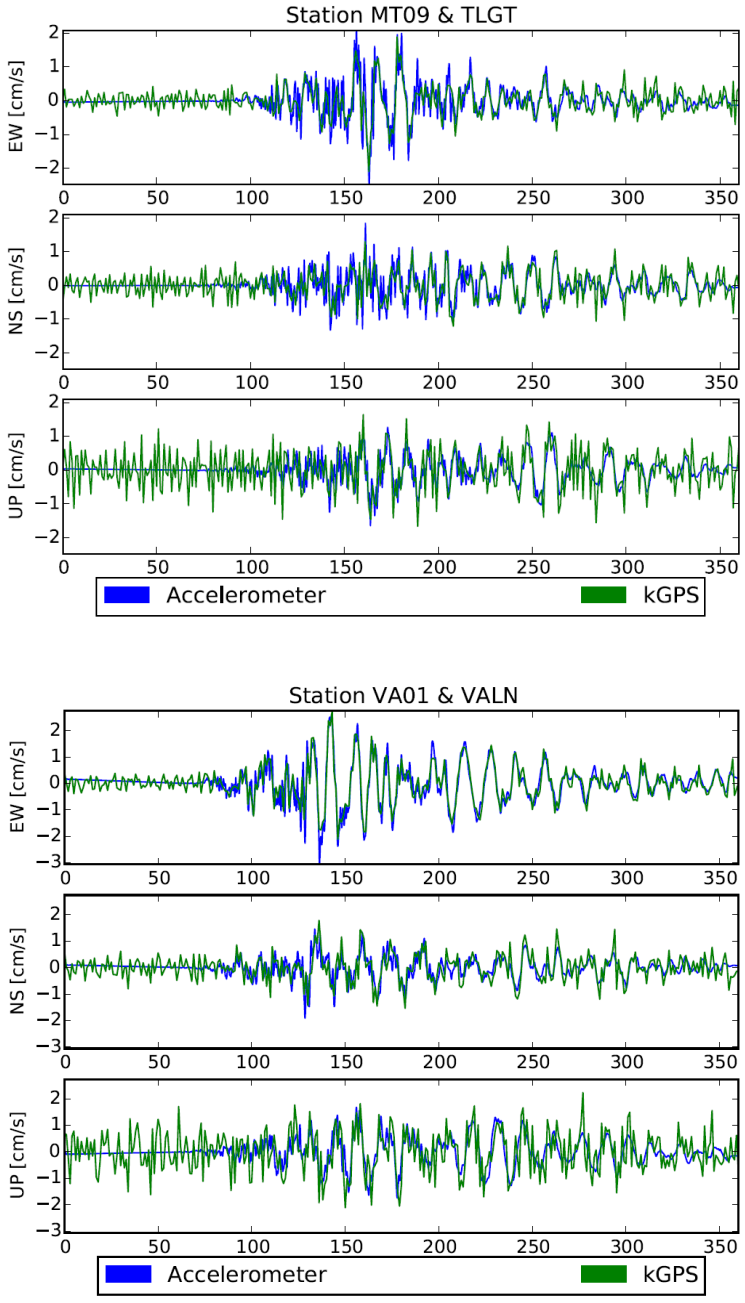

Figure 2.5. Velocity traces comparison for the 2015 Illapel main event.

2.4. Evidence of Site Effects from strong motion records

Strong motion records were analyzed to investigate possible evidences of site effects during the event. Of particular interest is the study of predominant frequency present in the strong ground motion. We used the Stockwell transform (Stockwell et al, 1996; Stockwell, 1999) to improve the resolution in the time domain and horizontal-to-vertical spectral ratio (HVSR) to estimate the predominant frequency. The results are shown in Figure 2.6 for stations C11O and CO03, left and right respectively. For each site, the panels represent: (a) HVSR computed at each point, using the S transform for each channel; we consider the total horizontal energy and divide it, on a point-by-point basis, by the vertical component (b) Percentiles computed for all the time points, showing the HVSR amplitude that represent the median; (c) Shows the total horizontal energy in the time domain, computed point-by-point as the square root of the sum of the squares of both components.

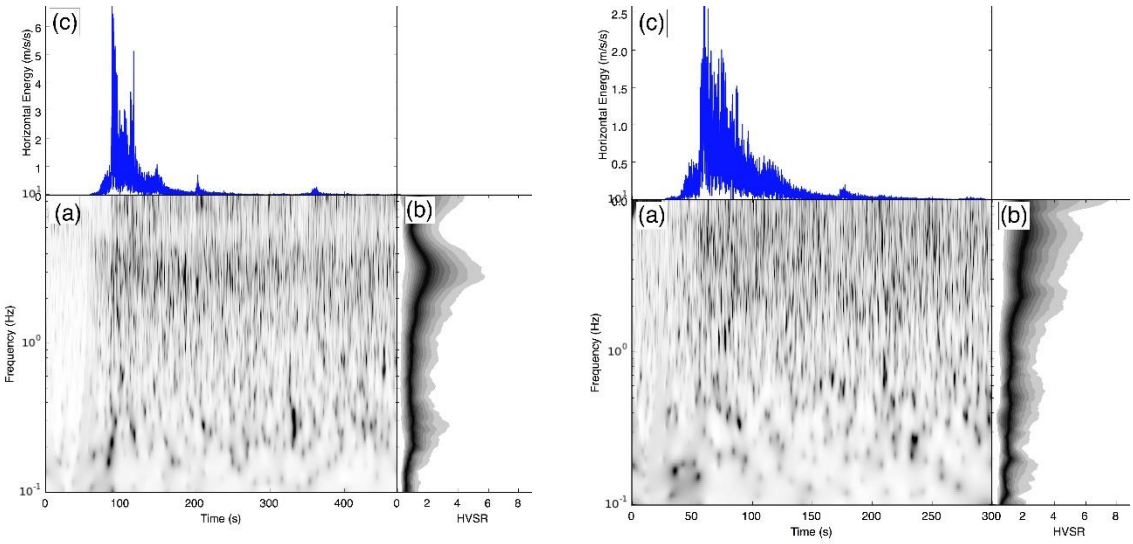

Figure 2.6. Results for C11O (left) and CO03 (right) of the horizontal-to-vertical spectral ration (HVSR) computed using the S transform. See text for details.

From Figure 2.6 we observe that C11O presents a peak at 3 Hz, present through all the strong motion record. On the other hand, CO03 presents a weak peak at about 8 Hz, but with a small amplitude; for these amplitudes we do not expect a predominant frequency. These observations agree with the results presented in Figure 2.4. There are larger residuals for C110 while CO03 shows only average residuals.

3. Damage to geotechnical systems

3.1. Retaining structures and damage to the seafront

The overall response of earth retaining structures in the region was satisfactory. At the places visited by the reconnaissance team, no significant damage was observed on gravity walls and other retaining structures supporting non-liquefiable backfills. Likewise, no evidence of seismically induced earth pressures damage was observed on MSE walls or building basements. In Coquimbo's shoreline as shown in Figure 3.1, a 10 m deep excavation supported on soldier piles and anchors was flooded by the tsunami; the ground shaking, however, caused no damage on the retaining system.

(a)

(b)

Figure 3.1. Flooded excavation in Coquimbo. No damage observed on the soldier piles and anchors (29.958151S; 71.337849W).

The ground shaking and the tsunami waves caused severe damage to Coquimbo's waterfront. The run-up depth in the bay was over 4.5 m and extended over a distance of ~500 m from the coast in some areas. As a result, several light-weight structures were washed away, lifelines were interrupted, and the tsunami inundation zone was left with several tons of tsunami debris causing the port and commerce along the shoreline to be completely shut down. Although access to the city port was denied to the GEER team, the observable damage was mostly due to flooding; no tilting was observed on lamp posts or cranes; authorities reported no significant damage on the container's terminal.

Adjacent to the port as shown in Figure 3.2, a 30 m long section of a gravity retaining wall failed, most likely due to the combined effects of tsunami waves, ground shaking and possibly liquefaction at the wall footing. The backfill material was made of a mixture of rock fragments and sand. Likewise in Figure 3.3, south of the port Costanera Avenue, the sand and rock fills that made the seafront were eroded and occasionally washed away by the waves.

Figure 3.2. Failure of gravity walls at Coquimbo's waterfront (29.951370S; 71.335721W).

3.2. Damage to bridge abutments

The Chilean Ministry of Public Works reported eight bridges damaged as a result of ground shaking. The most common damage patterns were the settlement of the bridge abutments, minor lateral spreading, banging of the concrete girders against the abutment structure, and damage to walkways, the bridge joints and elastomeric bearings. Five of these bridges were located on the Pan-American Highway, with the most severe damage observed in El Teniente

(a)

(b)

Figure 3.3. Sand and rock fills in Coquimbo's shoreline washed away by tsunami waves (29.958982S; 71.334789W).

Bridge, a 5-span RC structure build in the late 90s. The bridge's south abutment settled ~ 20 cm and displaced horizontally ~7 cm, leaving a residual deformation on the rubber bearings and large cracks in the approach pavement as shown in Figure 3.4. Traffic flow on the bridge was restored the following days after emergency asphalt ramps were built in the approach. A similar situation was observed in the Illapel II Bridge, in the city if Illapel (Figure 3.5). The north and south abutments settled ~10 cm, and the abutment slopes were affected by minor raveling. In both cases, no settlement was observed on the bridge piers, and soon after the earthquake, asphalt ramps were built to restore the traffic flow.

(a) 

(b) 

(c) 

Figure 3.4. Seismically induced displacements (vertical ~20cm, horizontal ~7cm) on the south abutment of El Teniente Viaduct on Route 5 (30.9956500S; 71.6306694W). (a) bridge approach before temporary repairs were made, photo taken on Sept. 17th, source: http://unionradio.net/dos-nuevos-sismos-sacuden-zona-afectada-por-terremoto-en-chile/ accessed on Oct. 9th 2015. (b) Asphalt ramp placed to mitigate the effects on moving vehicles, (c) Photo courtesy of Rosita Jünemann – CIGIDEN: deformed rubber bearings on the south abutment.

(a)

(b)

(c)

Figure 3.5. North abutment of Illapel II Bridge, Illapel (31.6316444S; 71.1565083W). (a) Settlement on 10-15 cm, source: http://www.ahoranoticias.cl/chile/santiago/153803-mop-difunde-mapa-actualizado-de-puentes-y-rutas-afectadas-por-el-terremoto.html, accessed on September 20th 2015. (b) Asphalt ramp, (c) raveling on abutment slopes and damaged sidewalk.

Other bridges inspected showed only slight damage or no damage at all. For instance, the Amolanas Viaduct in Route 5, equipped with shock absorbers, and one of the tallest bridges in South America, underwent no structural or geotechnical damage. Evidence of liquefaction was observed in the river bed of La Cebada Bridge, Figure 3.6; however, no settlement was observed in the bridge approach, only minor concrete spalling in the girders due to impact with the abutment structures.

(a)

(b)

Figure 3.6. Sand boils in the river bed of La Cebada Bridge, Route 5 (30.972870S; 71.642092W). Photo courtesy of Rosita Jünemann – CIGIDEN.

4. Rockfalls and landslides

Rockfall was widespread along roads and cut slopes within the zone of deformation of the earthquake rupture leading to complete and partial blockage of travel networks. No deep-seated landslides were observed although, with such a large area impacted, some are likely in regions that were not visited as part of the reconnaissance. Nevertheless, debris cones up to 200 m^3 impacted the Panamerican Highway (Route 5). Most areas were investigated both by road and on foot to document these effects. Field observations were supplemented by visual interpretation of aerial imagery using Google Earth.

4.1. Observations from Field Reconnaissance – Panamerican Highway (Route 5)

Mass-wasting was widespread across the rupture area as a consequence of the 2015 Illapel earthquake. Field reconnaissance was undertaken from immediately after the earthquake up to one week after. A focus of this investigation was the important lifelines such as the Panamerican Highway (Route 5), a major modern highway that runs north-south and parallel to the coast in Chile. The highway is a divided into two, two-lane northbound and southbound routes that run through hilly to mountainous terrain. Mass-wasting covered the road in sections (i.e., blocking the entire northbound or southbound lane), however, to our knowledge, no single rockfall covered both lanes in both directions. In addition, a number of other inland and seaward roads were also investigated.

The discussion of rockfall and landslides in this section will focus on Route 5 from Los Vilos north to immediately north of La Serena. Importantly, north of La Serena and outside of the main zone of deformation, slopes did not appear to be impacted as greatly as south of La Serena. From La Serena to La Higuera (~50 km north of La Serena) no slope stability issues were noted except for one sedimentary road cut at a river (Table 4.1, GPS RF10) before Route 5 makes a climb towards a major pass (Honda Pass) where Route 5 climbs approximately 600 m above sea level with a number of major cut slopes. There was no evidence for any slope stability issues along Route 5 on the climb to Honda Pass. This demonstrates a correlation between the location of surface deformation during the earthquake and slope stability distribution during this earthquake (i.e., north and south of the zone of tectonic deformation during this earthquake, geotechnical effects were limited).

Numerous topples or slumps were observed in over-steepened road cuts in the weathered igneous rocks and sediments within this region even where retaining walls and other mitigation structures were in place. In a number of occasions mitigation measures (e.g., fences, etc.) failed to stop slope failures from covering the roads. Oftentimes these over-steepened cut slopes had estimated inclinations of ¼ H:1V or steeper and had estimated

heights from 5 to over 30 meters for the loess road cuts. Oftentimes the material formed a wedge on the road. Importantly, due to the number of observations, the reconnaissance focused on single examples that were estimated to be at least 3 m^3 in volume. Those smaller than this were not counted. In some locations, rockfalls occurred along bedding planes, however most rockfall occurred from cliffs composed of highly fractured and weathered igneous rocks which failed due to strong ground motion. Note that there are large areas along Route 5 that are flat and without road cuts through hills and of course these areas did not experience any rockfall or slope stability issues. A map showing some of the major examples along the roadway is shown in Figure 4.1 below.

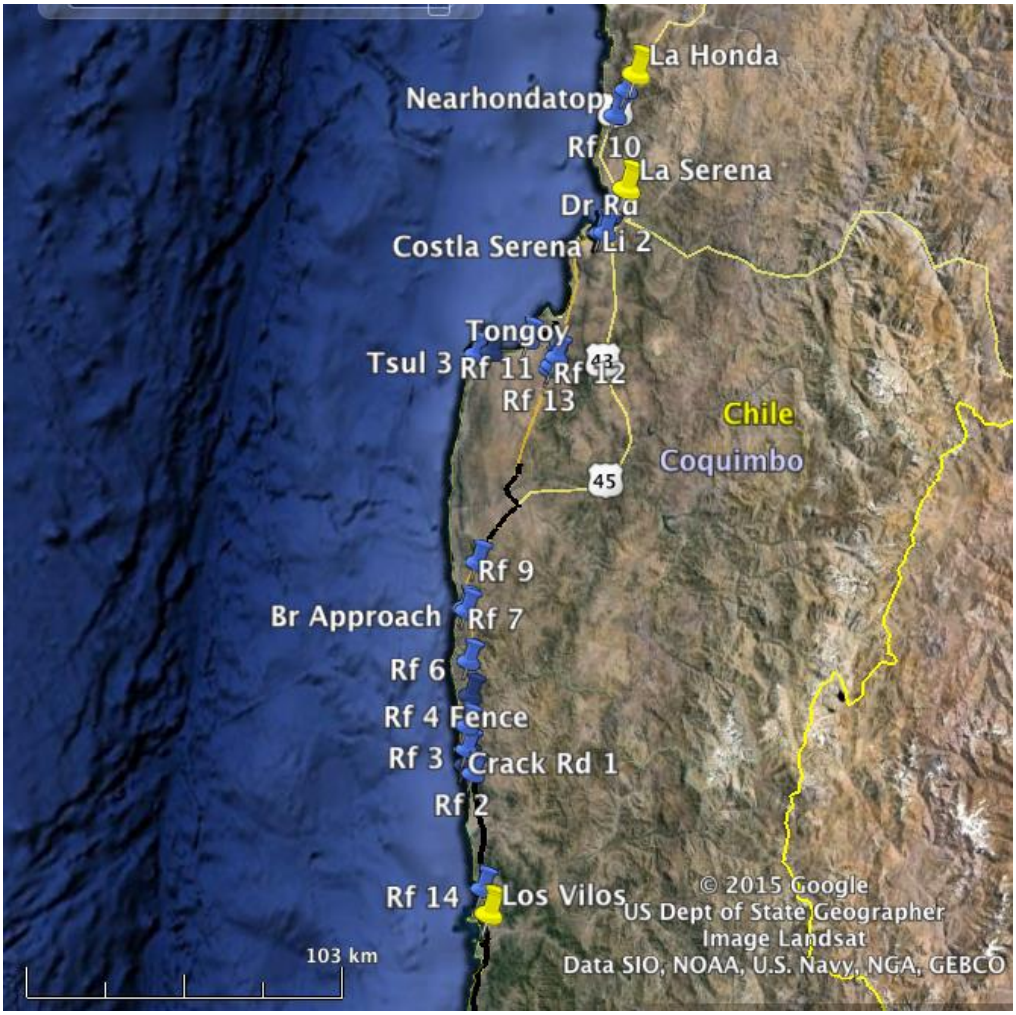

Figure 4.1. Google Earth map of main slope stability sites and associated GPS points (e.g., Rf 6) that impacted the Panamerican highway (Route 5). Yellow pins indicate the towns of Los Vilos and La Serena as well as the La Honda Pass from South to North. No notable rockfall occurred along Route 5 south of Los Vilos and none occurred north of RF10 which is ~30 km north of La Serena; most of the rockfall occurred in a ~ 250 km wide zone near the rupture patch.

4.2. North bound examples (Eastern lane of Route 5)

The examples below are given from South (Los Vilos) to North (La Serena) with the km (as noted from the road signs) marker noted – GPS locations are given as well. Where possible a qualitative estimate of volume (cubic meters – m^3) was made based on the distribution of the deposits combined with the geometry. Table 4.1 outlines the northbound main rockfall sites between Los Vilos in the South and La Serena in the North.

Table 4.1. Northbound observations of rockfall along the Pan Americana (Route 5) between Los Vilos in the South and La Serena in the North.

Route 5 (northbound) Km marker (South to North)	**Type**	**Origin of deposit (rock and/or sediment)**	**Volume estimate (m3)**	**Impact (Lane or road closed or destroyed mitigation structures)**	**GPS point name and coordinates (point locations shown on figure)**
291	Rockfall	Sediments with clasts	-	No damage, adjacent to lane	-
295	Rockfall	Angular blocks of rock	-	Rockfall barriers functioned well.	RF4 31.31521S 71.59444W see photos below
305	Rockfall	Intact blocks of rock (1-1.5 m^3)	Deposit 1: 20 Deposit 2: 25	Blocks went through the barriers and covered the road	RF5 31.23193S 71.58976W see photos below
308	Rockfall	Poorly consolidated rock	Deposit 1: 3 Deposit 2: 3	Debris cone at base on edge of road	
316	Rockfall	Sediments with clasts up to 1 m^3	>40	Rockfall barriers destroyed	RF6 31.13957S 71.60428W see photos below
334	Rockfall	Rock and sediments	80	Rockfall barriers destroyed	RF7 31.00348S 71.62430W see photos below
338	Rockfall	Rock and sediment.	-	The deposit covered part of the right lane	-
341	Rockfall	Rock	5	Did not cover the road, on the side	-
349.5	Rockfall	Unconsolidated sediments	3	Did not cover any lanes	-
368.5	Rockfall	Unconsolidated sediments	-	Did not cover any lanes	-
377-379	Rockfall	Unconsolidated sediments	-	Did not cover any lanes	-
508	Rockfall	Rock blocks from 1-2 m^3.	10	No observed damage	RF10 29.62911S 71.27890W

Field photos to document some of the sites outlined in Table 4.1 are shown below.

Figure 4.2. Km 295 northbound lane, looking south showing how the rockfall mitigation fences functioned well here and protected the road (GPS RF4: 31.31521S; 71.59444W).

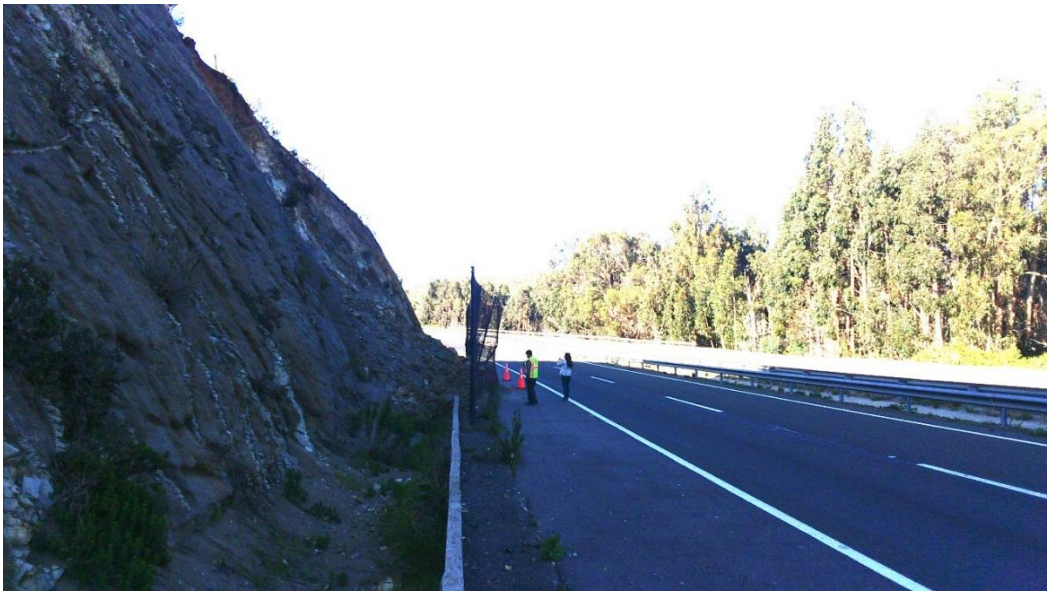

Figure 4.3. Km 295 northbound lane showing how the rockfall mitigation fences functioned well at this location and protected the road (GPS RF4: 31.31521S; 71.59444W).

Figure 4.4. Km 305 northbound lane looking north showing how the rockfall fences failed during a cut slope collapse (GPS RF5: 31.23193S; 71.58976W). Note the fresh rockfall in the foreground, behind the fence) of the photo which then builds to a large debris cone in the background.

Figure 4.5. Km 305, northbound lane Route 5 showing failed rockfall mitigation fences (debris in the road had previously been cleaned up by highway department (GPS RF5: 31.23193S; 71.58976W).

Figure 4.6. Km 316, northbound lane, slope failure impacted the northbound Route 5 and destroyed the mitigation fences closing one lane. Note excavator clearing the road (GPS RF6: 31.13957S; 71.60428W).

Figure 4.7. Km 334, northbound lane, rock slope failure looking north. Rockfall mitigation fences were destroyed on the northbound Route 5 with closure of both lanes after earthquake and one lane for at least 10 days later (GPS RF7: 31.00348S; 71.62430W).

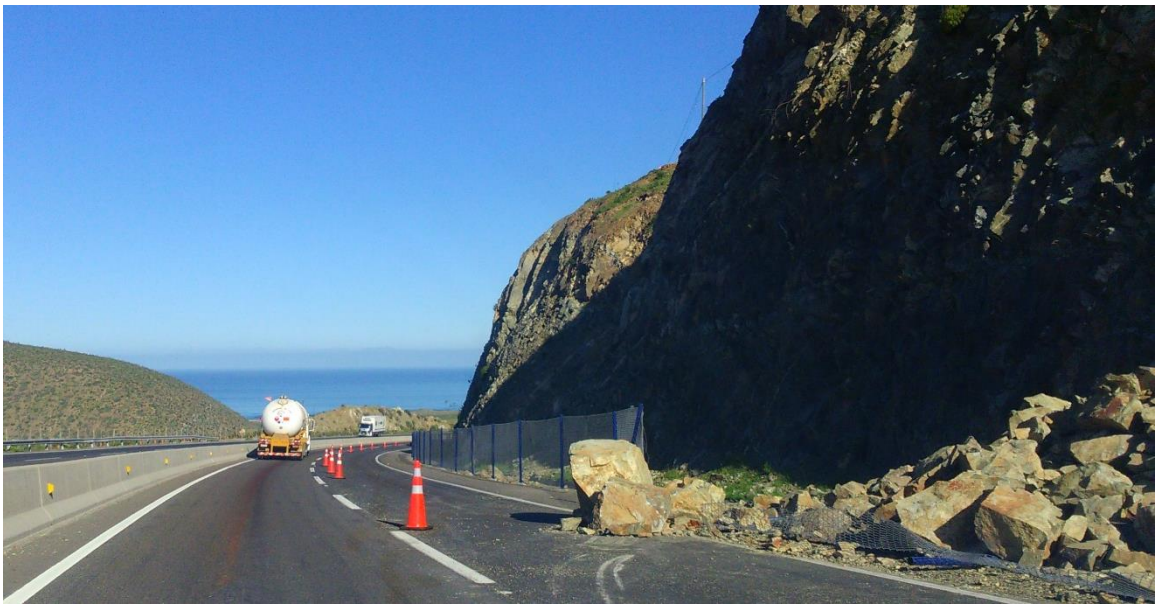

Figure 4.8. Km 334, northbound lane, rock slope failure looking north. Rockfall mitigation fences were destroyed. Note the large size angular blocks (1-2 m3) (GPS RF7: 31.00348S; 71.62430W).

Figure 4.9. Km 508, northbound lane, alluvium (boulders), that fell from the road cut (looking south). Some of these boulders were previously in the road and pushed into the drainage (GPS RF10: 29.62911S; 71.27890W).

4.3. Southbound examples (Western lane of Route 5)

During reconnaissance, estimates were taken at almost every occurrence of rockfall in the southbound lane in order to develop an estimate of the overall volume of rockfall generated along cut slopes during this earthquake. The main observations are summarized in Table 4.2.

Table 4.2. Southbound observations of rockfall along the Pan Americana (Route 5) between immediately north of La Serena in the North to Los Vilos in the South. Note that over 1000 m^3 of debris is estimated to have been falling on the southbound lane.

Route 5 (southbound) Km marker (North to South)	Type	Origin of deposit (Rock and/or Sediment)	Volume estimate (m3)	Impact (Lane or road closed or destroyed mitigation structures)	GPS point name (point locations shown on figure)
510	Rockfall	Sediments with alluvial blocks	5	No observed damage	-
505-508	Rockfall	Sediments with alluvial blocks.	10	No observed damage	
480	Rockfall	Rocks up to 2 m3	-	No observed damage	-
422	Rockfall	Unconsolidated sediments (poorly lithified coquina) up to 0.5 m3 diameter	5	No observed damage	RF11 30.29719S 71.40219W
419	Rockfall	Unconsolidated sediments	-	One lane southbound closed	RF12 30.31941S 71.41332W
418	Rockfall	Unconsolidated sediments	4	No observed damage	RF13 30.33138S 71.41932W
378	Rockfall	Blocks within sediments up to 1 m3 diameter, sections of collapse throughout	Deposit 1: 2 Deposit 2: 8 Deposit 3: 15 Deposit 4: 20	No observed damage	-
377	Rockfall	Bocks up to 0.5 m3	5	No observed damage	-
376	Rockfall	Unconsolidated sediments	15-20	No observed damage	-
369	Rockfall	Unconsolidated sediments	50	No observed damage	-
368	Rockfall	Unconsolidated sediments	Deposit 1: 10 Deposit 2: 5	No observed damage	-

361	Rockfall	Bedrock blocks up to 1 m3	Deposit 1: 50 Deposit 2: 3 Deposit 3: 60 Deposit 4: 7 Deposit 5: 10	Mitigation structures destroyed and one lane closed southbound	-
350	Rockfall	Extremely weathered rock and blocks	Deposit 1: 3 Deposit 2: 10 Deposit 3: 100 (likely double in size pre-cleaning)	Complete destruction of the mitigation structures. Very large slope failure with complete closure of the southbound two lanes of the highway. Deposit (3) continued into the northbound lane	RF9 30.87033S 71.60181W See photo below
349	Rockfall	Bedrock blocks	Deposit 1: 10 Deposit 2: 10 Deposit 3: 15	Rockfall protection intact and worked here	-
338	Rockfall	Unconsolidated sediments	20 (initially more than 100 m3 based on discussion with workers cleaning site and marks on road.)	One lane closed southbound	30.970396S 71.642938W See photo below
328.5	Rockfall	Unconsolidated sediments	2	No observed damage	-
295.5	Rockfall	Poorly consolidated bedrock	50	No observed damage	-
291.5	Rockfall	Poorly consolidated bedrock	6	No observed damage	-
289	Rockfall	Poorly consolidated bedrock	Deposit 1: 4 Deposit 2: 15 Deposit 3: 7 Deposit 4: 200	Lane closed.	-
287	Rockfall	Unconsolidated sediments	~150 - 200	Lane closed	RF3 31.37990S 71.58963W Photograph below
280	Rockfall	Fine-grained sediments	40	No observed damage	RF2 31.44367S 71.56376W Photograph below
243	Rockfall	Unconsolidated sediments	Deposit 1: 10-15 Deposit 2: 5	Lane closed	RF1
227	Rockfall	Blocks	2 to 3	No observed damage	-

The below figures show a few examples of field conditions as outlined in the Table 4.2.

Figure 4.10. Km 350, southbound lane (photo taken looking north from northbound lane) slope failure impacted the northbound Route 5 and destroyed the mitigation fences closing the entire southbound lane. Note the debris in the median between lanes (GPS RF9: 30.87033S; 71.60181W).

Figure 4.11. Km 338-339, southbound lane half closed from extensive slope collapse along Route 5. Field photograph looking north from the northbound lane. Cones indicate the closed southbound lane.

Figure 4.12. Km 287, southbound lane (photo looking north from northbound lane). Slope failure closed entire southbound lane, (note debris in median between lanes and excavator clearly the deposit). Deposit was estimated at 150-200 m3 (based on discussions with clearing crew and evidence on the ground) (GPS RF3: 31.37990S; 71.58963W).

Figure 4.13. Km 287, southbound lane (photo looking north from northbound lane). Slope failure closed entire southbound lane, (note debris in median between lanes and excavator clearly the deposit). Deposit was estimated at 150-200 m3 (based on discussions with clearing crew and evidence on the ground). Although not related to the slope failure note the cracks in the road due to slope settlement to the East in the foreground (GPS RF3: 31.37990S 71.58963W).

Figure 4.14. Km 280, southbound lane (photograph looking west from northbound lane). Rockfall closed one lane, damaged street light and exit sign (GPS RF2: 31.44367S; 71.56376W).

Figure 4.15. Km 280, southbound lane (photograph looking north from the southbound lane). Rockfall closed one lane, damaged streetlight and exit sign (GPS RF2: 31.44367S 71.56376W). Note that much of the deposit had been cleared prior to this photo being taken.

4.4. Rockfall observed on inland roads east of Route 5

Several inland roads were visited, including asphalted routes D-55, D-71, D-81, D-85, and dirt Routes D-75 and D-951 which run along the Choapa River (Figures 4.16. and 4.17). These roads cross hilly terrain and the fluvial transverse valleys that run east-west in the region, in some areas the roads run parallel to nearly vertical cliffs. The earthquake caused widespread damage to steep cut-slopes on sedimentary rocks and weathered igneous rocks, temporarily blocking traffic on one or two lanes. No deep-seated slope failures were observed in the area.

Figure 4.16. Map (from Google Maps) showing inland routes of D-75, D-85, D-81, east and northeast of Los Vilos.

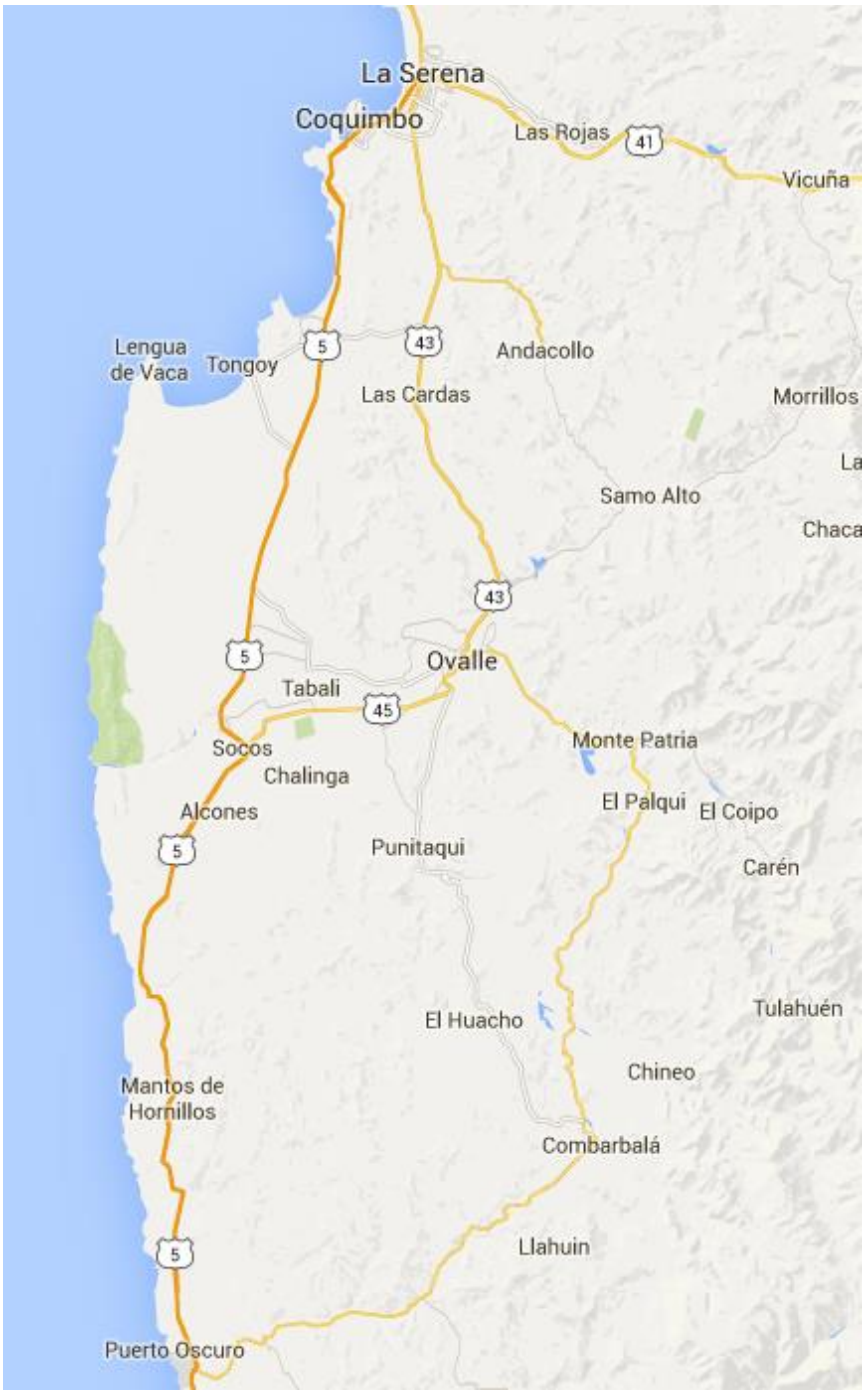

Figure 4.17. Map (from Google Maps) showing inland routes of D-55 (which runs east out of Ovalle and loops back to Puerto Oscuro in the south. Puerto Oscuro is the location where rockfall was observed imbedded in a residential home.

At the time of the reconnaissance (one week after the main shock) most asphalted roads had been plowed off and the traffic was fully restituted; only a few rural roads remained blocked due to large rockfall. Several sections in Route D-85 had been previously reinforced wire meshes and barriers to prevent rockfall from blocking the road. In general, these systems performed well as they caught the loose soil and small blocks of fractured rock, but in some locations the wire mesh fences did not hold.

Figure 4.18. Mass-wasting in westbound of route D-85 (31.77599S; 71.32873W).

Figure 4.19. Road plowing on route D-85 (31.7683S; 71.32676W).

(a)

(b)

Figure 4.20. Rockfall on route D-951 on the south rim of Choapa River (31.6234472S; 71.388122W), maximum block sizes over $1m^3$. This secondary road had been partially cleared at the time and traffic was allowed.

Figure 4.21. (Photo courtesy of Alondra Chamorro – CIGIDEN). As a result of massive rockfall, traffic was discontinued on Route D-75, north rim of Choapa River (31.59S; 71.41W).

(a)

(b)

Figure 4.22. (Photo courtesy of Alondra Chamorro – CIGIDEN). Rockfall on Route D-75, north rim of Choapa River, temporarily blocked the road (31.59S; 71.41W).

(a)

(b)

Figure 4.23. (Photos courtesy of Felipe Rivera – CIGIDEN). Rockfall and minor raveling on Route D-71. Traffic allowed (31.41S; 71.47W).

4.5. Rockfall impact on other structures

Single boulder rockfall, emanating from both natural slopes and engineered slopes was likely common although the effect on built structures was likely limited. However one location that was visited during the GEER reconnaissance was Puerto Oscuro (~50 km north of Los Vilos and on the coast). This site was visited to explore tsunami run up and while there it was noted that one large boulder (~3-4 m^3) fell off of the hillslope and imbedded itself in the roof of a house next to the beach at Puerto Oscuro (GPS Rock Casa). With a number of small communities in the region of the rupture in areas with steep slopes, it is likely that other single boulders impacted the built environment although oftentimes these examples like there are rare to document. Figure 4.24. shows the boulder that was embedded in the back of the house in Puerto Oscuro as a team was trying to extract it.

Figure 4.24. Photograph showing a boulder (with two men attaching slings to it), imbedded in the back of a property in Puerto Oscuro that fell from a natural slope above the property (31.42234S; 71.59291W).

5. Liquefaction

5.1. Liquefaction and lateral spreading

In documenting the effects of major earthquakes it is important to note areas both with and without impact on built structures to better understand the geotechnical and geologic factors that control co- and post-seismic ground deformations. Liquefaction during the 2015 Illapel main shock and aftershocks was not extensive, however, local damage was observed in structures including bridges, drainage systems (i.e., sewers), roads, powerlines, and buildings. All areas were investigated both by road and on foot to document the occurrence (or lack thereof) of liquefaction. Field observations were supplemented by visual interpretation of aerial imagery using Google Earth imagery. A combination of low-groundwater levels (due to semi-arid climate and drought) combined with limited geologic environments with fine-grained sediments in the area contributed to the limited distribution of observed liquefaction from the 2015 Illapel earthquake sequence.

5.2. Observations from Field Reconnaissance – Liquefaction

In contrast to mass-wasting, which was widespread across the rupture area as a consequence of the 2015 Illapel earthquake, liquefaction occurrence was much more localized and limited to areas with near-surface groundwater and suitable sediments for liquefaction susceptibility. Field reconnaissance was undertaken from immediately after the earthquake up to two weeks after the earthquake. No liquefaction was observed south of Tongoy although Los Vilos and other sites along the coast were assessed. Most evidence was found between Tongoy and La Serena (Figures 5.1 and 5.2).

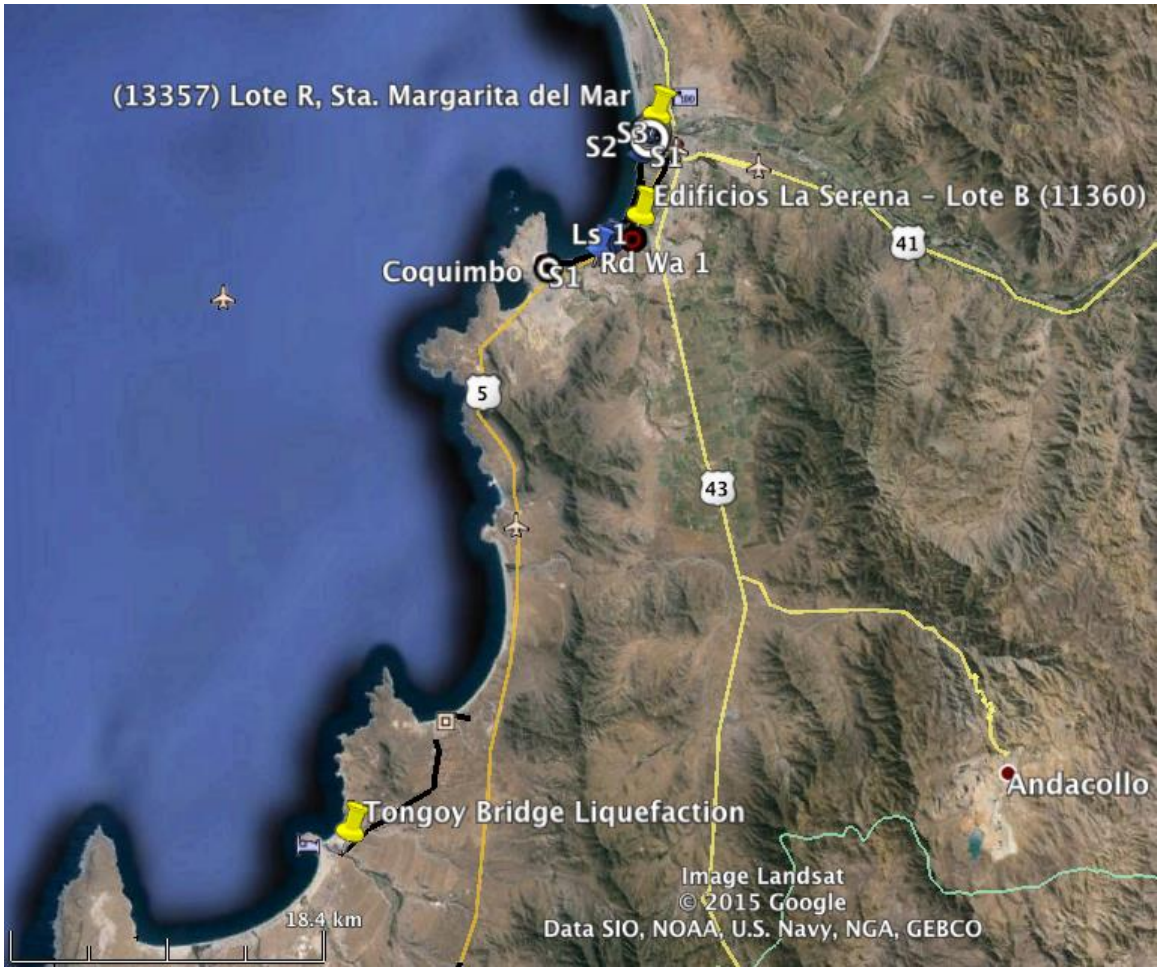

Figure 5.1. Google Earth map of main liquefaction sites and associated GPS points (e.g., Tongoy Bridge Liquefaction). No notable liquefaction was observed by the GEER team south of Tongoy. Population density and thus built structure density is higher here than other areas near the fault rupture place, so thus the likelihood for observing liquefaction is higher in these areas. Also important, having structures built in low-lying, geologically young areas, (e.g. Holocene deposits in this case, coastal lagoons, and beaches near La Serena) also increases the likelihood for liquefaction-induced damage.

Figure 5.2. Google Earth map of main liquefaction sites and associated GPS points in the La Serena and Coquimbo region. Main observations were near the Li 2 Start GPS points as well as the El Faro along the coast to the north.

Six main sites are documented here (Table 5.1) and are discussed in detail below. Importantly, a number of these sites were visited post-earthquake with equipment for shear wave velocity characterization.

Table 5.1. Main Sites

Liquefaction site number	Location (GPS point name) and coordinates	Manifestation of liquefaction	Additional information	Shear Wave velocity data (Y/N)	Impact (Impact on built structures)
1	S2 29.896866S 71.268320W	No Liquefaction observed. Santa Margarita del Mar building complex that during geotechnical site investigations showed potential for liquefaction.	No evidence for liquefaction observed at surface. Site was excavated prior to construction and thus perhaps engineered fill backfilled the site (speculation).	Y	No impact visible.
2	Faro 1 29.90541S 71.27411W	Lighthouse/El Faro of La Serena. Evidence for differential settlement due to liquefaction, however site impacted by tsunami. Test on the south side, in the middle of wall south of the lighthouse tower on the beach (adjacent to El Faro, on the southern side as close as possible to the El Faro's south wall). Further CPT work here will confirm.	El Faro was built around 1952-1953. External walls were damaged in a previous event (unknown if due to tidal scour or previous liquefaction event) and walls were patched with concrete and repainted. New failures post-2015 earthquake evidenced through open fractures in the external walls. Adjacent structures showed differential settlement with damage to structure (with rebar).	Y	Outer El Faro walls broke open along previous failure planes due to a combination of differential settlement due liquefaction and wave scour. Adjacent structure damaged as well due to settlement. Future CPT testing here (planned) will help determine liquefaction susceptibility at this location.
3	Liq 1 29.95368S 71.30173W	This is the main N-S road along the coast south of the Casino between La Serena and Coquimbo. Liquefaction was observed here as well as lateral spreading, however the site was impacted by tsunami. Further CPT work here will confirm.	Ground conditions are coastal beach sand with high water table. Possibly further altered after tsunami. Faint evidence for sand boils at the surface in additional to horizontal displacements towards free face at coast. Site is adjacent and south of where the Los Pescadores road meets the Costanera (coastal Road).	Y	Road destroyed over 20 m section long and rebuilt week of Oct 5.

4	Li 2 29.95068S 71.29456W	Test on eastern side of road (or through road) adjacent to floating sewer). Differential settlement due to liquefaction and lateral spread. Eastern side of Los Pescadores (N-S road) where it meets Padre Gabriel Gonzalez Videla). Between La Serena and Coquimbo. Surface water channel, filled with water and adjacent to road likely contributed to site effects.	Over 600 m long section with clear evidence of liquefaction and lateral spreading parallel to and adjacent to Los Pescadores street (between Peñuelas Norte and Peñuelas Sur streets). Here the Southeastern side of the road shows vertical subsidence and Southeastern displacement towards the low-lying coastal lagoon/swamp area. In addition to the floating services (man holes up to 80 cm above pre-earthquake levels), there was subsidence of the native and/or filled ground below the road (20-30 cm). Notably, further deformation was noted two weeks after the main shock with road parallel cracks in the road as well as open fresh cracks in the soil that was not present one week earlier. This was likely due to further liquefaction triggered during aftershocks.	Y	Water services (sewer pipes) above ground due to subsidence and floatation although appeared to be still functioning although will have to be repaired. Unsure if they are leaking, etc. Powerline towers (concrete) tilted due to settlement.
5	D-420 Bridge 30.260784S 71.481196W	Bridge along the D-420 adjacent (southeast) of the new steel bridge. Failure observed (slumping due to settlement due to liquefaction). Test northeastern side of river/creek between the two bridges on the flat area. This location is just outside of Tongoy.	Bridge appeared to have been decommissioned prior to earthquake, with new steel structure located immediately to the west. However, the older bridge was clearly damaged during the earthquake (closer to epicenter than other sites near La Serena).	Y	Vertical settlement of the structure. Clear damage. Bridge was being removed/deconstructed week of Oct 5th.
6	Edificios La Serena 29.949781S 71.282109W	No evidence for liquefaction at this location. Development in La Serena with SPT evidence for liquefaction potential during site investigations pre-construction.	Site walkover post-earthquake showed no evidence for liquefaction of the surface nor impact on built structures. Discussion with site Engineer indicated that the top 5 m at the site was excavated and engineered fill was emplaced to prevent liquefaction.	N	No impact visible.

5.3. Liquefaction Site One – Santa Margarita del Mar building complex

At the Santa Margarita del Mar building complex no evidence of liquefaction was observed during the week of Oct 5. Figure 5.3 shows the shear wave velocity profiles and the H/V spectral ratios (Nakamura's technique).

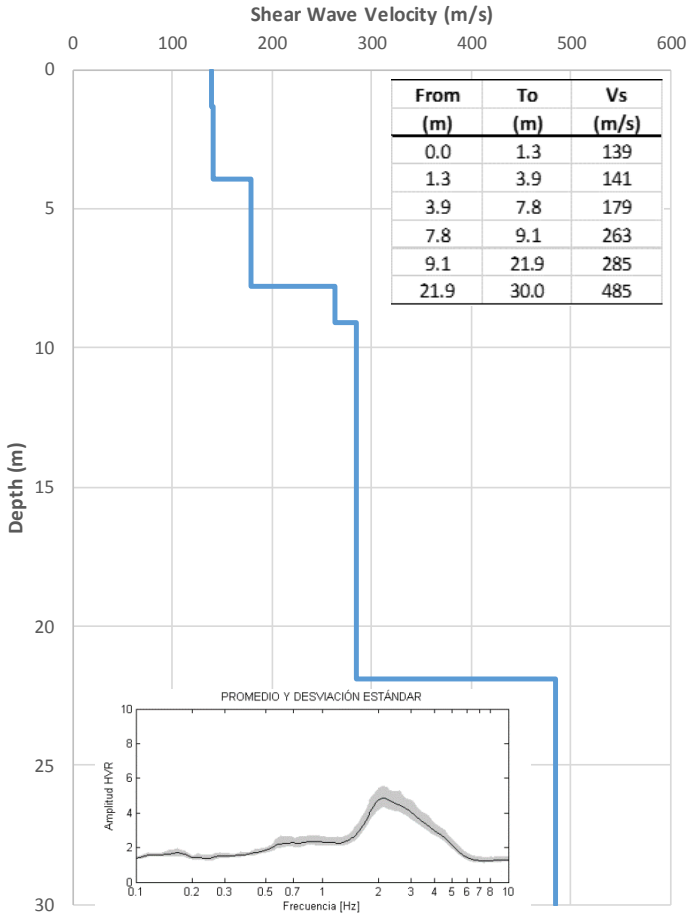

Figure 5.3. Shear wave velocity profiles and H/V spectral ratios at (29.896866S; 71.268320W).

5.4. Liquefaction Site Two – La Serena Lighthouse (El Faro)

As mentioned in Table 5.1, this is a site where liquefaction and lateral spreading may not have happened and if it occurred was likely altered by the tsunami afterwards. The site appeared to have liquefied based on the shear wave velocity data, subsided and then was afterwards washed away by the tsunami, however upcoming CPT results from this site will confirm what was suggested from the field evidence and V_s data. As shown in the photos, cracks from previous damage to El Faro (damage occurred sometime between 1953 and

2015), were fixed with concrete and painted over and were then re-opened during the recent earthquake. The adjacent building shows clear evidence for differential settlement during liquefaction. Planned CPT investigations will further assist with the liquefaction susceptibility at this location to allow a better characterization between damage due to scour of the foundation and from liquefaction during strong ground motions.

Figure 5.4. El Faro photograph looking north (29.90541S; 71.27411W). Note the break in the outer wall (i.e., change in angle indicated with the black arrow) where the western edge of the El Faro wall subsided with a westward tilt apparent at the top of the wall. This happened prior to this earthquake and was patched and painted over, however during the 2015 earthquake, cracks opened up along these fractures that suggest renewed subsidence.

Figure 5.5. El Faro outer wall (Western, adjacent to sea) showing open fractures due to differential settlement during liquefaction perhaps in conjunction with wave scour (29.90541S; 71.27411W).

Figure 5.6. Field photograph looking north from El Faro towards the adjacent structure that shows clear differential settlement (down to the Southwest) with damage to the arc. Scour from waves as well as liquefaction was likely at this site (29.90541S; 71.27411W).

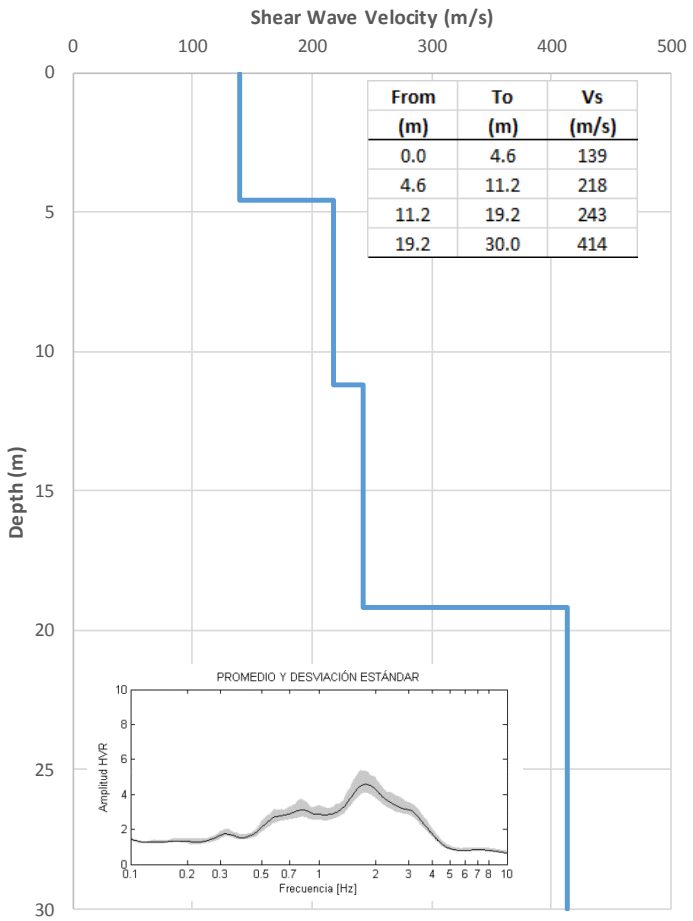

Figure 5.7. Shear wave velocity profiles and H/V spectral ratios at (29.90541S; 71.27411W). Liquefaction likely took place in the upper 5 m.

5.5. Liquefaction site three - main N-S road along the coast south of the Casino between La Serena and Coquimbo.

As mentioned in Table 5.1 this is a site where liquefaction and lateral spreading may have been altered by the tsunami afterwards. The site appeared to have liquefied, subsided and then was afterwards washed away by the tsunami.

Figure 5.8. Field photograph showing an area that likely experienced liquefaction and was then disturbed by the tsunami. Two-lane road formerly ran along the coast and was completely cut due to damage. Vertical relief from road surface to debris below is 1.5 to 2 m. Note tsunami debris in foreground near orange electric pipe (29.95368S; 71.30173W).

Figure 5.9. Field photograph next to the destroyed road with small mounds of sand that may have been sand boils (29.95368S; 71.30173W).

Figure 5.10. Field photograph looking toward Coquimbo that shows subsided walkway adjacent to where the road may have undergone liquefaction-induced subsidence and then was further washed away by the tsunami. Site was likely modified by tsunami immediately post event (29.95368S; 71.30173W).

Figure 5.11. Field photograph of the destroyed road location on October 5, after the road was repaired and fully functioning (29.95368S; 71.30173W).

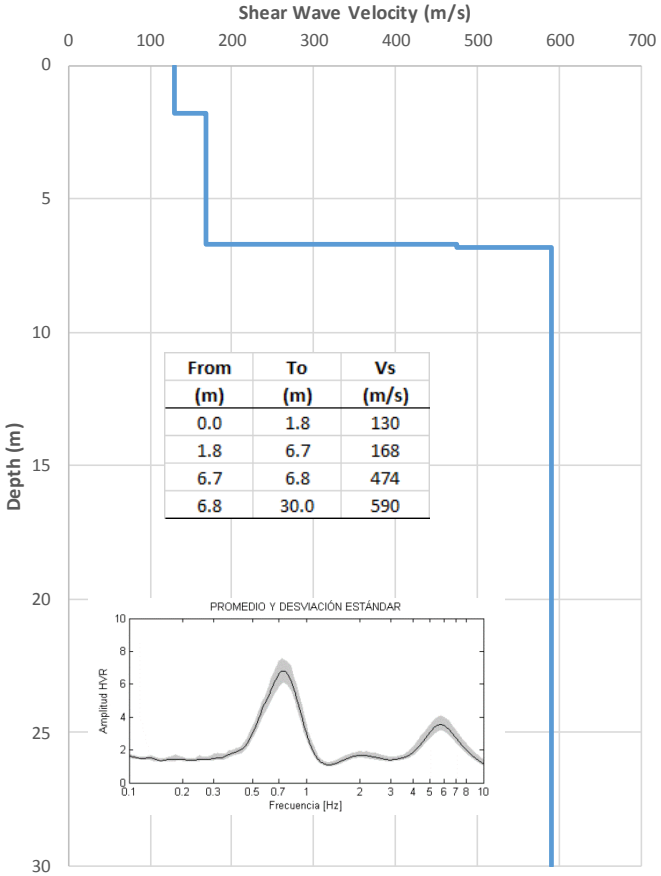

Figure 5.12. Shear wave velocity profiles and H/V spectral ratios at (29.95368S; 71.30173W). Liquefaction likely took place in the upper ~6 m.

5.6. Liquefaction site four – near coast in La Serena with lateral spreading and floating services

As mentioned in Table 5.1, this site exhibited evidence of liquefaction and lateral spreading over at least 600 m and parallel to the coast in La Serena. Here, liquefaction was evident with liquefaction-induced floating of concrete sewer services (i.e., flotation - raised sewer portals and raised pipes), vertical subsidence noted with cracked ground, normal (downward) faulted blocks of soil, and cracks within nearby roads and tilted power poles. The first observations here were taken one week after the earthquake while the sites were revised one week later (week of October 5, 2015), which showed continued deformation (likely due to numerous $M_w > 6$ aftershocks during this one-week period).

Figure 5.13. Field photograph looking north on Los Pescadores street (29.95068S; 71.29456W) showing the curb with horizontal separations of 5-10 cm (to the southeast), as well as vertical subsidence (at person's feet from 3-6 cm vertical).

Figure 5.14. Field photograph looking northeast along Los Pescadores street. Note services have floated to the surface (uplifting the soil in blocks on to the right of person). Sewer top is now 70 cm above around surface. Note the second sewer portal behind person. Ground subsidence is also clear with the ground subsiding 20-30 cm relative to the road at this location. Surface water channel (runoff) runs directly behind the main sewer portal and parallel with the road (29.95068S; 71.29456W).

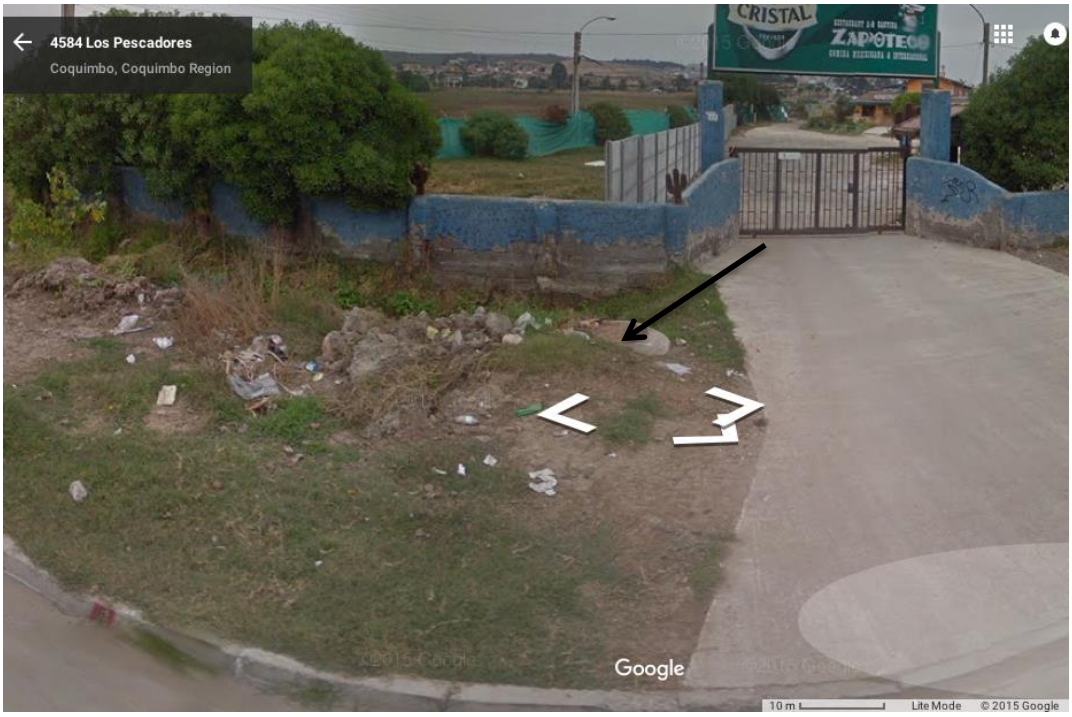

Figure 5.15. Google "Street View" of the same manhole cover seen in the previous figure pre-earthquake from ~ 4584 Los Pescadores (1 block southeast of the seaside). Note that it is flush with the ground surface and black arrow indicates manhole (29.95068S; 71.29456W).

The following observations are from the same site one week later (October 6-9).

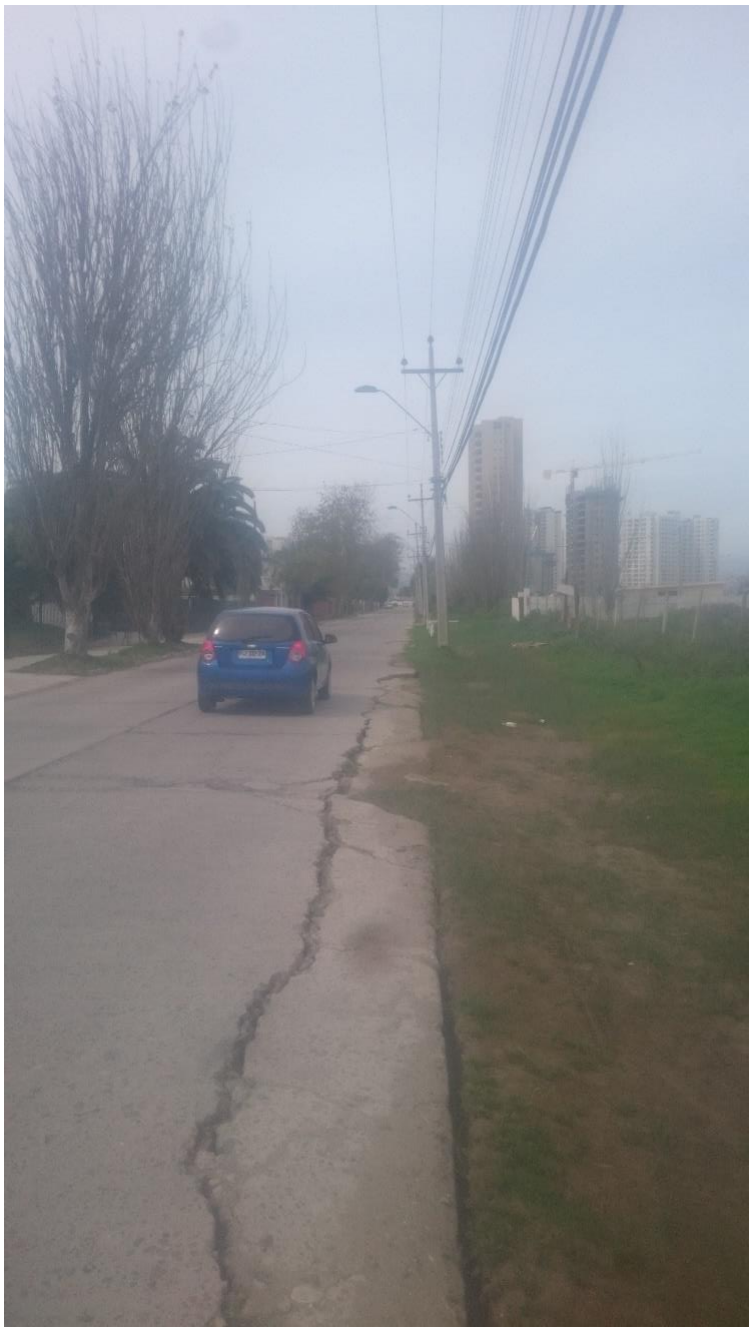

Figure 5.16. Field photograph looking north along Los Pescadores road. Note that the edge of the road has road parallel cracks where the road has failed to accommodate vertical subsidence and horizontal deformation of the soil during lateral spreading. Also note that the power lines in the back are tilted (29.95068S; 71.29456W).

Figure 5.17. Field photograph looking southwest along Los Pescadores street that shows floating services (on left) and vertical soil subsidence and lateral spreading. GPS is 15.0 cm long and 5.5 cm wide for scale. Horizontal displacements of the intact soil range from 2-20 cm here and vertical subsidence from 0 to 10 cm (29.95068S; 71.29456W).

Figure 5.18. Field photograph showing concentric fractures in the concrete roadway which are accommodating the vertical and horizontal soil deformation underneath. GPS is 15.0 cm long and 5.5 cm wide for scale. Note the soil in the cracks and plants growing which suggests these cracks formed during previous earthquakes here (i.e., liquefaction during previous events took place here, which caused the formation of the cracks). The soil and plants lived here until the 2015 earthquake caused another round of liquefaction and further lateral spreading and subsidence (29.95068S; 71.29456W).

Figure 5.19. Field photograph of same site as above showing concentric ring fractures in the concrete due to liquefaction induced subsidence. Photograph is looking Southwest along Los Pescadores street. GPS is 15.0 cm long and 5.5 cm wide for scale. Note that the ground pre-earthquake was level to the left (southeast) of the round and has now subsided 25-40 cm and been horizontally translated (29.95068S; 71.29456W).

Figure 5.20. Second floating service portal along Los Pescadores Street with ~35-40 cm of combined floating services and subsidence. Note the edge of the road in the background that was flush with the ground surface pre-earthquake (29.95068S; 71.29456W).

Figure 5.21. Field photograph of the same Los Pescadores street sewer portal however 8 days after the first photograph (and after a number of M_w 6+ aftershocks). Note that the services have continued to float and is now ~25 cm higher than the first photos (Black arrow indicates a line in the concrete portal that was below ground surface during first set of observations). The top of the manhole is also more tiled (>5 degrees) during this second set of observations. This shows that liquefaction occurred during some of the aftershocks of this sequence (29.95068S; 71.29456W).

Figure 5.22. Field photograph looking Southwest along Los Pescadores street with clear subsidence along normal faulted blocks in soil due to liquefaction and associated lateral spreading. Here vertical displacement is 5-20 cm and horizontal is 10-30 cm (29.95068S; 71.29456W).

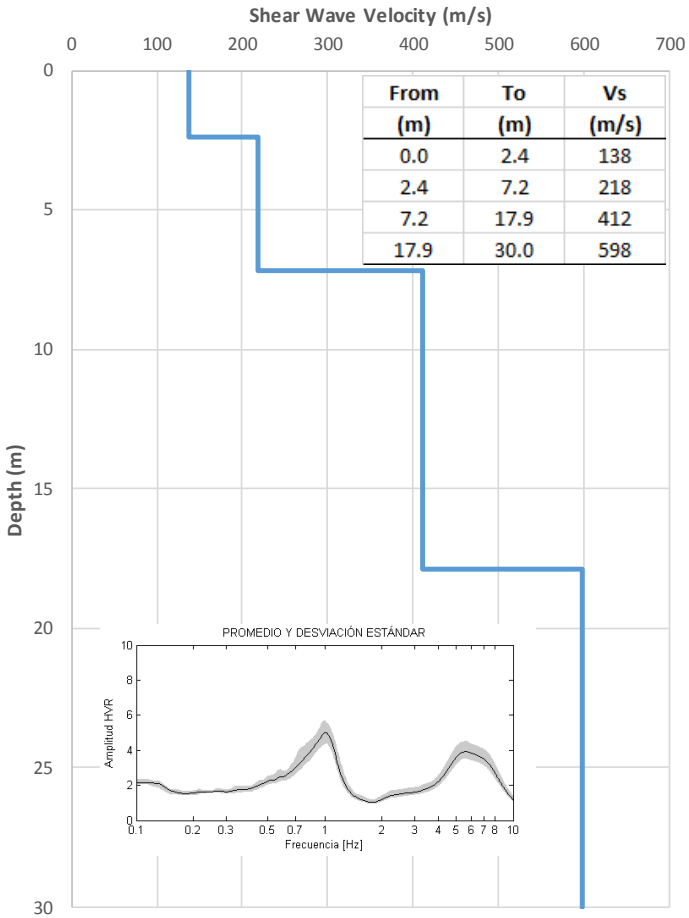

Figure 5.23. Shear wave velocity profiles and H/V spectral ratios at (29.95068S; 71.29456W). Liquefaction likely took place in the upper 2.5 m

5.7. Liquefaction site five – D-420 bridge near Tongoy

The D-420 Bridge crosses a river/estuary in the outskirts of Tongoy (< 1km north of town) whilst heading north towards La Serena. This bridge is <100 m East of the new steel bridge which was in place at the time of the earthquake. The replacement of this bridge prior to the earthquake with a new steel bridge suggests that the structural integrity of this bridge was suspected due to time, design, and or usage. Nevertheless, this bridge certainly was damaged during the event. As shown in the following photos, the bridge sheared off at the northern approach and dropped ~1.5 to 2 m below road level. This suggests liquefaction induced settlement and lateral spreading, which based on the fine-grained sediments and high water table seem likely.

Figure 5.24. Field photograph looking east of the D-420 Bridge. Northern end of the bridge has a vertical step where it failed during the earthquake likely during liquefaction (30.260784S; 71.481196W).

Figure 5.25. Field photograph looking south of the D-420 bridge. Northern end of the bridge has a vertical step where it failed during the earthquake, likely due to lateral spreading during liquefaction. People shown for scale (30.260784S; 71.481196W).

Figure 5.26. Field photograph looking south of the D-420 bridge. Northern end of the bridge has a vertical step where it failed during the earthquake – likely during liquefaction induced lateral spreading. Note the new steel bridge in the background on right (30.260784S; 71.481196W).

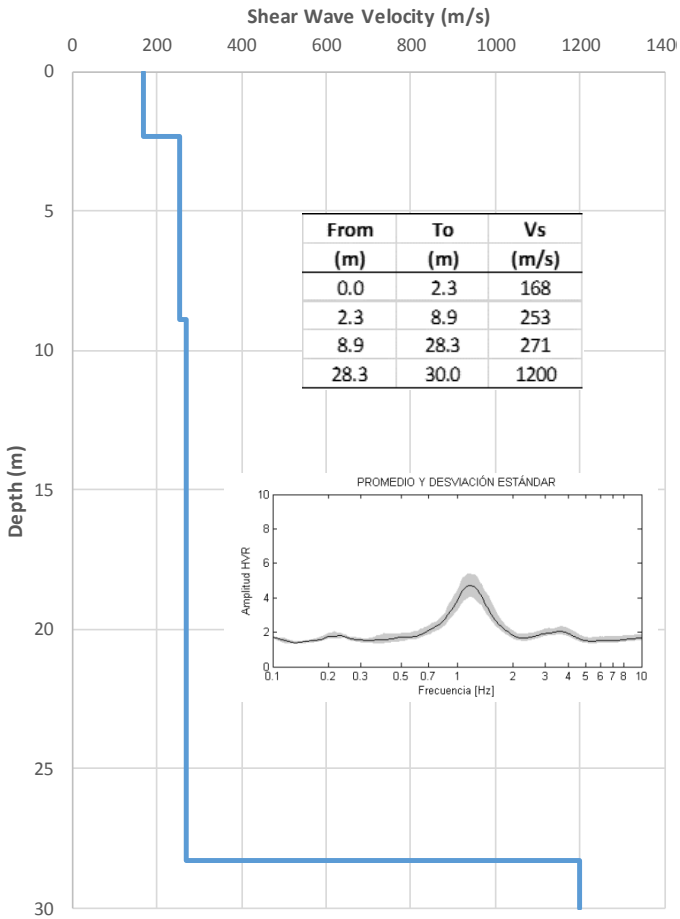

Figure 5.27. Shear wave velocity profiles and H/V spectral ratios at (30.260784S; 71.481196W). Liquefaction likely took place in the upper 2.5 m

5.8. Liquefaction site six – Edificios La Serena

Based on pre-earthquake site investigation data, liquefaction was expected at this site. However, no surficial signs of liquefaction were observed (based on visit on October 9). This could have been because the entire site was pre-excavated up to 4 m to 5 m deep and replaced with engineered fill, which replaced the native material and likely reduced liquefaction susceptibility in the upper 4 m to 5 m.

Figure 5.28. View of the site looking NW, as of October 9. No signs of liquefaction were observed. The pond is part of the project, and the building behind the pond towards the coast is under construction.

6. Tsunami effects

Tsunami waves were present along the coast of all of the rupture region of the Illapel earthquake. Along the coast, the impact of the tsunami was variable according the height reached by the waves. Tsunami heights were measured using a barometric altimeter calibrated at the moment of each observation and then corrected by tide effect considering the Chilean Navy Hydrographic and Oceanographic Service information (Servicio Hidrográfico y Oceanográfico de la Armada, SHOA, www.shoa.cl), yielding an error of ±0.5 m. The highest pervasive marks left by vegetation razed by the tsunami were recorded, but also traces of erosion on the beach, sand and boulder deposits and the impact on coastal locations. Two areas of maximum tsunami heights were observed associated to the two main rupture patches, one reaching 5-6 m just to the south of the epicenter, and the other reaching as high as 10-11 m to the north of the epicenter (Figure 6.1). According to witnesses, the tsunami reached the coastline no more than 5-7 minutes after the earthquake along the epicentral zone.

Figure 6.1. Razed dunes and vegetation and accumulation of boulders evidencing the effect of the tsunami waves at El Sauce (30.55S; 71.69W). Note 4x4 truck and people for scale.

Regarding the impact of the tsunami on buildings, waves swept the area of Coquimbo in the north, reaching up to 6 m above sea level and producing strong erosion along the coast including the main coastal road (Avenida Costanera) as well as flooding of buildings (Figure 6.2 to 6.11) and failure of gravity retaining walls. The waves inundated a number of areas further afield from the coast as could be seen with debris lines on fences and other structures. Similar effects were observed in small fishing localities situated along the coast of the epicentral region, like Huentelauquén, Caleta Sierra (El Maitén), Caleta el Sauce, Caleta Talcacura and Caleta El Totoral. At Caleta Sierra, for instance, tsunami waves reached +4 m, strongly impacting the lower area of the embayment and causing destruction of several houses and fisher boats (Figure 6.13). In the Southern end of the rupture area, near Los Vilos, a number of houses adjacent to the beach were completely destroyed or damaged beyond repair (e.g., Figure 6.14).

Figure 6.2. Strong erosion at the coastal border of caused by the tsunami in the area of Coquimbo (29.95342S; 71.29860W).

Figure 6.3. Tsunami erosion and scour along Avenida Costanera, Coquimbo (29.960589S; 71.328062W).

Figure 6.4. Avenida Costanera split in two, Coquimbo (29.959600S; 71.332964W).

Figure 6.5. Coquimbo's port and borderline. Large fishing boats tossed onto the streets (29.952126S; 71.336148W).

Figure 6.6. Small fishing boat on Avenida Costanera. Army and military equipment deployed in the area soon after the earthquake (29.960629S; 71.333272W).

Figure 6.7. Aerial view of Avenida Costanera showing the erosion on the coastline (29.958274S; 71.335126W).

Figure 6.8. Flooding of the first story at Costa Mansa building (29.960144S; 71.332698W). Estimated run-up depth of 4.5 m.a.s.l. The structure, a 26 story RC shear wall building, was not damaged by the ground motion, however basic utilities (water, gas, electricity) were discontinued and residents were forced to move out.

Figure 6.9. Flooding of *Liceo Diego Portales's* gymnasium located in Avenida Costanera, Coquimbo (29.953371S; 71.336161W). The structure is a steel frame building which sustained no structural damage from the earthquake; non-structural components such as division panels, peripheral fences and utilities were washed away by the waves

Figure 6.10. Flooded buildings at Avenida Costanera in the area of Coquimbo and tsunami debris.

Figure 6.11. Avenida Costanera, Coquimbo. Neighbors improvised tents and emergency kitchens (*Olla Común*) outside their flooded building while cleaning operations continued.

Figure 6.12. Field photograph showing the location of tsunami inundation ~100 m from the coast in La Serena on Los Pescadores Road (near some of the liquefaction sites). Note the level of the tsunami wave here was less than 20 cm high as indicated by the debris line along the fence indicated with the blue arrow. Similar types of evidence of minor inundation was seen over hundreds of meters in this area.

Figure 6.13. Caleta Sierra (El Maitén) embayment, were tsunami waves reached +4 m, strongly impacting the lower area and causing destruction of several houses and fishing boats (31.15S; 71.66W).

Figure 6.14. Field photograph looking east of a house at street level along the Costanera Av. in Los Vilos that was destroyed by the tsunami waves. Note that the house is tilted, and the backyard of the house is visible where the back wall was washed away. Many of the houses along this road were completely destroyed or greatly damaged by the waves. The beach here is just behind the photographer on the other side of the road (31.906212S; 71.500804W).

Abrahamson, N., Gregor, N., and Addo, K. (2015). BC Hydro Ground Motion Prediction Equations for Subduction Earthquakes. Earthquake Spectra In-Press. DOI: http://dx.doi.org/10.1193/051712EQS188MR

Akkar, S., & Bommer, J. J. (2006). Influence of long-period filter cut-off on elastic spectral displacements. Earthquake engineering & structural dynamics, 35(9), 1145-1165.

Angermann, D., Klotz, J., and Reigber, C. Space-geodetic estimation of the Nazca-South America Euler vector. Earth and Planetary Science Letters, 171(3):329 – 334, 1999. ISSN 0012-821X. DOI: http://dx.doi.org/10.1016/S0012-821X(99)00173-9.

Baez, J.C. (2015) Kinematic inversion of the Illapel 2015 earthquake of GNSS instruments. CSN Internal Report.

Bastías, N., and Montalva, G.A. (2015). Chile Strong Ground Motion Flatfile. Submitted to Earthquake Spectra.

Beck, S., Barrientos, S.E., Kausel, E., Reyes, M., 1998. Source characteristics of historical earthquakes along central Chile subduction zone. J. South Am. Earth Sci. 11, 115e129.

Comte, D., Eisenberg, A., Lorca, E., Pardo, M., Ponce, L., Saragoni, R., & Suárez, G. (1986). The 1985 central Chile earthquake: a repeat of previous great earthquakes in the region? Science, 233(4762), 449-453.

Del Campo, F., and Baez, J.C. (2015) Estimation of a slip model of the Illapel 2015 earthquake using static deformations from GPS. CSN Internal Report.

DeMets, C., Gordon, Richard G., Argus, Donald F., and Stein, Seth. Effect of recent revisions to the geomagnetic reversal time scale on estimates of current plate motions. Geophysical Research Letters, 21(20):2191–2194, 1994. ISSN 1944-8007. DOI: 10.1029/94GL02118.

Dura, T., Cisternas, M., Horton, B.P., Ely, L.L, Nelson, A.R., Wesson, R.L, and Pilarczyk, J.E., 2015, Coastal evidence for Holocene subduction-zone earthquakes and tsunamis in central Chile, Quaternary Science Reviews, V., 113, p. 93-111.

Heinze, B. Active intraplate faulting in the forearc of north central Chile (30◦–31◦s): implications from neotectonic field studies, GPS data, and elastic dislocation modelling. Scientific technical report, Geo-forschungszentrum Potsdam, 2003.

Kelleher, J., 1972. Rupture zones of large South American earthquakes and some predictions. J. Geophys. Res. 77, 2087e2103.

Le Roux, J.P., Olivares, Danisa M., Nielsen, Sven N., Smith, Norman D., Middleton, Heather, Fenner, Juliane, and Ishman, Scott E. Bay sedimentation as controlled by regional crustal behaviour, local tectonics and eustatic sea-level changes: Coquimbo formation (miocene–pliocene), bay of Tongoy, central Chile. Sedimentary Geology, 184(1–2):133–153, 2006. ISSN 0037-0738. doi: http://dx.doi.org/10.1016/ j.sedgeo.2005.09.023.

Lomnitz, C., 1970. Major earthquakes and tsunamis in Chile during the period 1535 to 1955. Int. J. Earth Sci. 59, 938e960.

Martınez, R. Hallazgo de foraminíferos miocénicos cerca de Puerto Aldea, Bahía de Tongoy, Provincia de Coquimbo, Chile. Revista Geológica de Chile, 8:65–78, 1979.

Melnick, D., Bookhagen, B., Strecker, M.R., Echtler, H.P., 2009. Segmentation of megathrust rupture zones from fore-arc deformation patterns over hun- dreds to millions of years, Arauco peninsula, Chile. J. Geophys. Res.: Solid Earth 114 (B1).

Nishenko, S. (1991). Seismic potential for large and great interplate earthquakes along the Chilean and Peruvian margins of South America: a quantitative reappraisal. J. Geophys. Res. 90, 3589–3615.

SERNAGEOMIN, Geologic map of Chile: Digital version, scale 1:1.000.000. Servicio Nacional de Geología y Minería, Santiago, Chile. 2003.

Stockwell, R.G. (1999). S-transform analysis of gravity wave activity from a small scale network of airglow imagers. PhD thesis, University of Western Ontario, London, Ontario, Canada.

Stockwell, R.G., L. Mansinha, y R. P. Lowe (1996). Localization of the complex spectrum: the S transform. IEEE Trans. Signal Process, 44, 998–1001.

Tassara, A. (2010). Control of forearc density structure on megathrust shear strength along the Chilean subduction zone. Tectonophysics 495, 34–47.